POLITECNICO DI TORINO

Master's Degree in Aerospace Engineering

Master's Degree Thesis

Minimum-propellant low-thrust trajectory optimization for orbit lowering in LEO via indirect methods

Supervisors

Prof. Manuela BATTIPEDE

Dr. Luigi MASCOLO

Candidate

Vincenzo DE ANGELIS

December 2025

Abstract

The growing interest in low-altitude operations for scientific and commercial applications has strengthened the relevance of orbit-lowering campaigns in Low Earth Orbit (LEO). Operating in this environment offers substantial advantages, including enhanced spatial resolution for Earth observation and natural compliance with space debris mitigation guidelines. However, the significant atmospheric drag and strong coupling between orbital and aerodynamic dynamics make trajectory optimization a complex task.

This work addresses the problem of optimizing a low-thrust orbital descent using an indirect approach based on Optimal Control Theory (OCT). The governing equations are formulated as a Two-Point Boundary Value Problem (TPBVP), derived from the necessary conditions of optimality given by Pontryagin's Maximum Principle. The resulting nonlinear system is solved iteratively through a Differential Correction (DC) procedure, which updates the initial conditions until the prescribed terminal constraints are satisfied.

The dynamical model is based on a medium-fidelity Two-Body Problem (2BP) formulation including atmospheric drag effects, evaluated through a one-dimensional interpolation of precomputed atmospheric density data. The numerical implementation has been developed in Python with particular attention to convergence stability and sensitivity to initial conditions.

The results confirm that the indirect optimization framework effectively identifies minimum-propellant trajectories for controlled orbit lowering under low-thrust propulsion. The methodology developed in this thesis provides a robust foundation for future studies focused on guidance, control, and end-of-life operations in LEO and Very Low Earth Orbit (VLEO) regimes.

Acknowledgements

I would like to express my sincere gratitude to Professor Luigi Mascolo for his constant and dedicated support during the development of this thesis. His profound expertise in the field, together with the enthusiasm conveyed in every discussion, fostered a stimulating and collaborative research environment that made this study particularly engaging.

I would also like to thank Professor Manuela Battipede for giving me the opportunity to carry out this thesis; her astrodynamics course laid the foundations for this work.

A special thanks goes to my family, whose unwavering support has been a constant presence throughout this long academic journey.

"Stammi a sentire: non ti fidare di chi ti dice che solo con le tue forze puoi farcela. Ci vuole anche ciorta, come diciamo qua."
– Luciano De Crescenzo

Table of Contents

List of Tables

List of Figures

Acronyms

LEO
Low Earth Orbit

ESA
European Space Agency

OCT
Optimal Control Theory

OCP
Optimal Control Problem

GAs
Genetic Algorithms

TPBVP
Two-Point Boundary Value Problem

MPBVP
Multi-Point Boundary Value Problem

BCs
Boundary Conditions

Chapter 1

Introduction

1.1 Preface

Space missions have always been constrained by one fundamental limitation: the finite amount of propellant that can be carried onboard. Propellant availability directly affects both the payload mass that can be delivered into orbit and the duration or versatility of the mission itself. The relationship between payload, propellant, and velocity change is governed by the *Tsiolkovsky rocket equation*, which reveals the exponential penalty associated with propellant mass. Even modest reductions in propellant requirements can therefore translate into substantial gains in payload capacity or mission lifetime.

$$\frac{m_p}{m_0} = 1 - \exp\left(-\frac{\Delta V}{I_{sp} g_0}\right) \tag{1.1}$$

In this equation, ΔV denotes the total velocity variation required by the mission, I_{sp} is the specific impulse of the propulsion system, and g_0 is the standard gravity. The equation highlights a key challenge in astronautics: achieving the necessary orbital maneuvers while minimizing fuel consumption. This consideration has guided space system design since the earliest days of space exploration and remains a cornerstone of modern mission planning.

In recent decades, the aerospace sector has experienced rapid evolution, driven by both scientific ambitions and commercial opportunities. On the scientific front, increasingly precise Earth observation and geophysical missions demand finely optimized orbits to enhance the accuracy of their measurements. Examples include ESA's GOCE and Swarm missions, which operated in low and very low Earth orbits to maximize sensitivity to gravitational and geomagnetic variations. Such missions demonstrate how orbital altitude directly influences data resolution and scientific return.

At the same time, the commercial space industry has undergone a profound transformation. The proliferation of private operators and the advent of large satellite constellations in Low Earth Orbit (LEO) have intensified the demand for efficient, low-cost orbital maneuvers. Operators now routinely consider controlled orbit lowering not only as a means of improving imaging resolution and communications performance, but also as a strategy for end-of-life disposal and compliance with international debris mitigation policies. The transition from traditional high-altitude operation to Very Low Earth Orbit (VLEO) regimes represents both a technical challenge and an opportunity for innovation.

A pivotal technological enabler of these developments is the advent of low-thrust electric propulsion (EP) systems, such as ion and Hall-effect thrusters. Unlike conventional chemical engines, which provide short but powerful thrust impulses, EP systems deliver continuous low accelerations over long durations, achieving far higher specific impulses. This allows for efficient propellant use during gradual orbital changes such as altitude lowering, inclination correction, or drag compensation. The combination of EP and precise numerical optimization enables new mission profiles that were previously impractical with chemical propulsion.

In parallel, the field of trajectory optimization has advanced significantly. Modern mission analysis now routinely employs a wide range of optimization techniques—direct, indirect, and evolutionary methods—to determine control laws that minimize propellant consumption or transfer time. Among these, the *Indirect Methods* (IM) based on Optimal Control Theory (OCT) are particularly effective in identifying theoretically optimal trajectories by solving boundary value problems derived from first-order necessary conditions of optimality.

In this framework, the study of low-thrust orbital maneuvers has gained renewed importance, especially for missions operating in the lower layers of LEO and in VLEO. The combined use of high-efficiency propulsion and indirect optimization techniques provides an analytical foundation for designing orbital transfers that balance energy efficiency, mission robustness, and operational constraints.

This thesis builds upon these concepts by focusing on the optimization of a low-thrust orbit-lowering maneuver in LEO, representative of contemporary trends in both scientific and commercial spaceflight. The objective is to identify minimum-propellant trajectories through the application of indirect optimization methods, demonstrating how the integration of advanced control theory and electric propulsion can enhance the overall efficiency of space missions, enabling greater payload capacity and extending the scope of achievable operations.

1.2 Field of study

Orbit lowering campaigns in Low Earth Orbit (LEO) are increasingly regarded as a strategic and enabling tool in both scientific and commercial space missions. Recent operational practices illustrate how lowering a spacecraft's altitude after initial deployment or during its operational life can deliver significant performance enhancements.

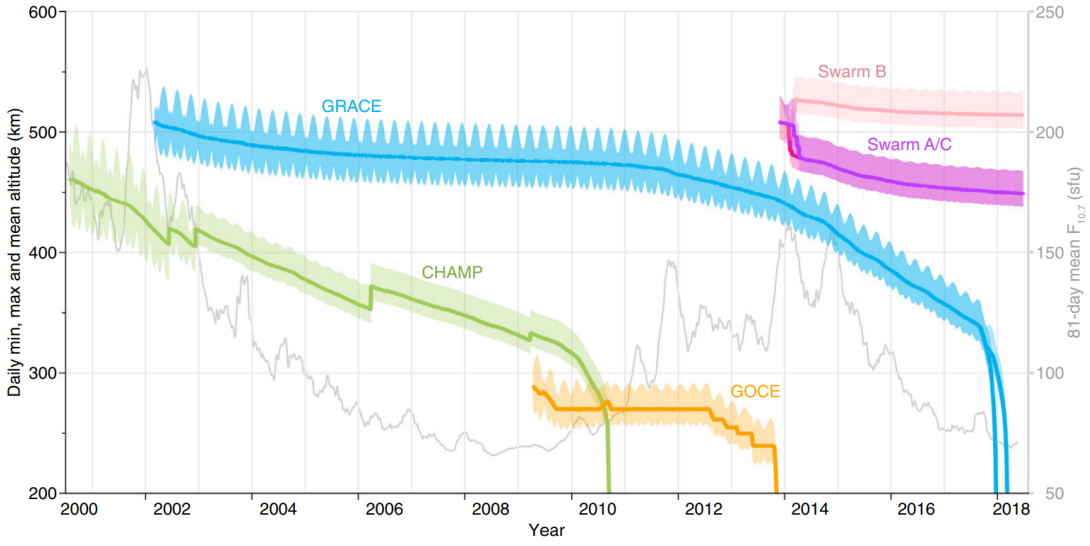

Figure 1.1: Altitude evolution of CHAMP, GRACE, GOCE, and Swarm satellites. Figure reproduced from March et al. [2] for academic and illustrative purposes only. © 2018 Elsevier Ltd.

For example, the European Space Agency (ESA) reports that the Earth-observation company Planet Labs lowered its SkySat constellation from approximately 500 km to 450 km in early 2020, enabling native optical resolution of about 50 cm. This demonstrates how a modest reduction in altitude can directly improve imaging capability [3, 4]. Similarly, ESA's GOCE mission was injected at around 295 km, subsequently operated near 270 km and in its final phase descended further to about 229 km in order to maximise gravity-field mapping precision [5]. These cases underscore the growing use of altitudinal manoeuvres to exploit proximity to Earth in order to enhance mission metrics.

Satellite	CHAMP	GRACE-A, -B	GOCE	Swarm-A, -C	Swarm-B
Operator	DLR	NASA/DLR	ESA	ESA	ESA
Launch date	Jul. 2000	Mar. 2002	Mar. 2009	Nov. 2013	Nov. 2013
End of mission	Sept. 2010	Oct. 2017	Oct. 2013	–	–
Initial altitude	460 km	505 km	270 km	470 km	530 km
Inclination	87.3°	89.0°	96.7°	87.4°	87.8°

Table 1.1: Mission characteristics for the CHAMP, GRACE, GOCE, and Swarm satellites [2].

More broadly, the concept of Very Low Earth Orbit (VLEO)—typically considered as orbital altitudes from about 200 km to 450 km—is gaining traction in the space community. Investigations by Crisp et al. [6] indicate that operations in VLEO enable better spatial resolution for a given optical payload (or conversely reduced payload mass for the same performance), improved signal-to-noise ratio for radar and lidar sensors, enhanced communications link budgets, and potentially shorter latency in data transmission. ESA further emphasises that VLEO offers lower launch cost per unit of capability, a more benign radiation environment (permitting the use of terrestrial-grade electronics) and a self-cleaning feature due to natural atmospheric drag, which contributes to post-mission disposal compliance. Additional research corroborates these benefits, showing that for Earth-observation missions, descending from higher LEO to altitudes below 400 km could reduce platform mass by up to 75 % and lower development or manufacturing cost by roughly 50 % when enabled by appropriate VLEO-tailored technologies [7].

The attractiveness of VLEO is particularly relevant for modern Earth-observation constellations, telecommunications networks and sensing platforms seeking higher performance with lower cost. For instance, the European Defence Agency (EDA) recently launched the *LEO2VLEO* project—a manoeuvrable constellation capable of operating between LEO and VLEO—targeting altitudes in the 250–350 km range for high-resolution military and dual-use applications [8]. Commercial operators share this interest: Planet's aforementioned SkySat campaign exemplifies how a small altitude adjustment can directly translate into competitive advantage and improved market value for imaging services. Industry analyses have also pointed out that altitude is one of the key cost drivers in satellite imaging, where operating closer to Earth can enable simpler optics, lighter spacecraft and higher-quality data products at reduced mission cost [6, 7].

However, operating in VLEO or executing orbit-lowering manoeuvres imposes notable engineering and operational challenges. The denser residual atmosphere at those altitudes increases aerodynamic drag, leading to greater fuel expenditure for station-keeping or faster orbital decay if left uncompensated. Atomic-oxygen erosion progressively degrades surfaces and optical coatings, requiring dedicated protection or materials specifically designed for low-altitude environments [9].

Thermal cycling and aerodynamic torques also affect attitude stability, while the denser environment modifies surface charging and aerodynamic moments [6]. From the propulsion standpoint, long-duration low-thrust systems—such as electric propulsion (EP)—are well suited for gradual lowering and drag compensation, but their limited thrust levels impose extended manoeuvre durations that must be traded against mission timelines [10, 11].

Novel concepts such as atmosphere-breathing electric propulsion (ABEP) propose to sustain thrust using the rarefied atmospheric particles as propellant, potentially enabling continuous operation in VLEO without carrying large fuel reserves. Although still in the experimental phase, such concepts are expected to make future long-duration VLEO missions feasible and sustainable [11]. These advances highlight that electric propulsion remains the key technological enabler for orbit-lowering and drag-compensation campaigns, particularly when combined with high-fidelity aerodynamic modelling and adaptive control techniques.

From a regulatory and sustainability perspective, orbit lowering and VLEO operations deliver significant contributions. Spacecraft operating in this regime naturally comply with most debris-mitigation requirements, since the elevated drag ensures deorbit within months or a few years after mission completion. This aligns with the *IADC Space Debris Mitigation Guidelines*, which recommend a post-mission lifetime shorter than 25 years [12]. Moreover, reducing the number of long-lived objects in high LEO helps alleviate congestion and enhances the long-term sustainability of satellite operations. The synergy between improved observation performance and responsible orbital management is one of the main reasons behind the renewed interest in orbit-lowering campaigns.

Scientific missions have also demonstrated the feasibility and scientific return of very-low orbits. GOCE's drag-free control system and aerodynamic design allowed continuous operation near 250 km, producing gravity-field data with unprecedented spatial resolution [5].

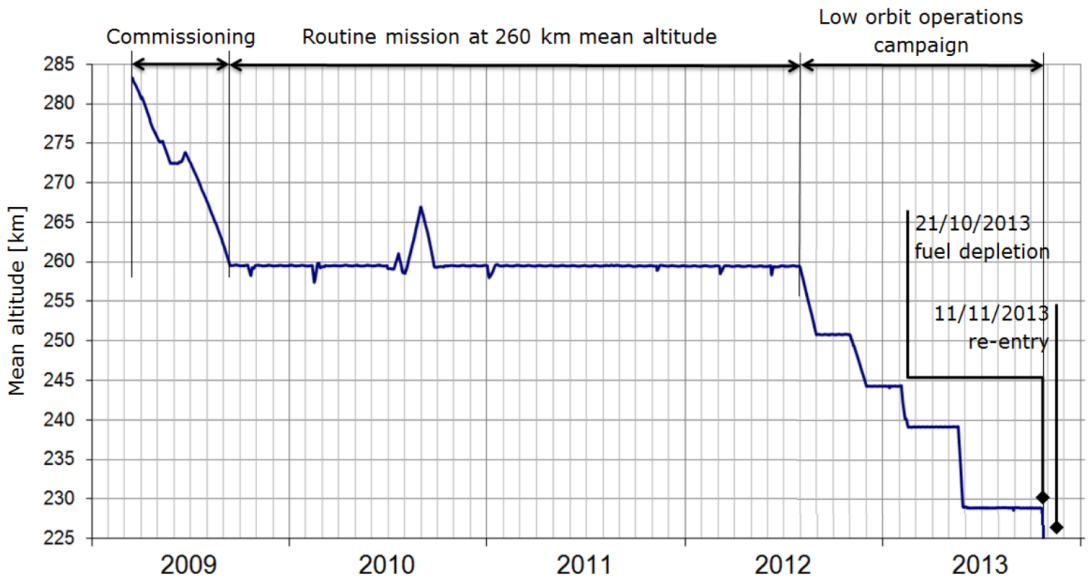

Figure 1.2: Evolution of GOCE satellite mean altitude from commissioning to re-entry (2009–2013). Source: European Space Agency [13].

ESA's Swarm constellation employed a differential-altitude strategy—one satellite near 530 km and two at 460 km, later descending toward 300 km—to improve the sensitivity of geomagnetic measurements [14]. Such missions provide operational templates for future low-altitude campaigns, showing how coordinated orbit lowering can enhance the quality of scientific data.

In parallel, commercial and defence entities are exploring similar strategies. Planet Labs, Maxar and other Earth-observation companies now routinely analyse the trade-off between optical performance, drag, and propulsion cost when defining operational altitudes. ESA's and EDA's recent initiatives, including the *LEO2VLEO* demonstrator, confirm a wider institutional effort to mature technologies and standards for sustainable operations in this emerging orbital band [8]. These trends suggest that orbit lowering is no longer merely an end-of-life strategy, but an integral part of active mission optimisation and value generation.

Within this framework, the scenario examined in this thesis—a lowering manoeuvre from 500 km to 490 km altitude—occupies a relevant position at the interface between conventional LEO operations and VLEO-enabled performance. By targeting the upper limit of the VLEO regime, the present work seeks to harness the benefits of proximity (higher imaging resolution, improved signal-to-noise ratio, better communication geometry, and enhanced disposal behaviour) while mitigating the most severe environmental and operational constraints associated with very low altitudes. The ultimate goal of this research is to identify minimum-propellant descent trajectories using low-thrust electric propulsion, via indirect optimisation

methods. This approach combines the physical insight of Optimal Control Theory with modern numerical techniques, providing a framework capable of balancing performance, efficiency and sustainability in future orbit-lowering missions.

1.3 Dissertation overview

The following provides a brief overview of the chapters that constitute this dissertation.

- Chapter 2 outlines the dynamical framework adopted for the study. It first introduces the reference systems and the essential coordinate transformations, then presents the structure of the dynamic model. Finally, it summarizes the perturbative effects considered in the simulations.
- Chapter 3 presents the theoretical and computational framework of Optimal Control Theory applied to trajectory optimization. After introducing direct, indirect, and heuristic approaches, the fundamental equations for optimality and control are derived. The formulation is extended to multi-point problems and solved via a single-shooting differential correction scheme. The developed methodology is then applied to a Low Earth Orbit (LEO) descent trajectory optimization case study.
- Chapter 4 presents the application of the developed optimal control framework to a set of representative orbit-lowering scenarios in Low Earth Orbit. The analysis includes both ideal and drag-perturbed cases, allowing the impact of atmospheric drag on the optimal solution to be assessed. Different thrusting strategies are investigated and compared in terms of propellant consumption, mission duration, and orbital evolution.
- Chapter 5 concludes the thesis by summarising the achieved results and evaluating the effectiveness of the proposed approach. Possible methodological and modelling extensions are finally discussed as directions for future work.

Chapter 2

Dynamic models

This chapter introduces the dynamic context within which the optimization process takes place. The first part provides a brief description of the reference systems involved in the analysis together with the main coordinate transformation required, while the subsequent segment delves into the actual dynamic model. The chapter concludes with a description of the perturbing effect included in the simulation.

2.1 Reference systems

The set of an origin, a fundamental plain and an orthonormal right-handed triad, called reference frame (RF), constitutes a Reference System (RS). The choice of an inertial or non-inertial RS depends on the specific scenario. In this analysis, it is not necessary to take into account pseudo-accelerations that make a system non-inertial, such as the Coriolis force or the centrifugal force in rotating RFs. The motion of a satellite relative to the earth is easily described in an inertial RS in different types of coordinates, such as Cartesian or polar. In the present thesis, the geocentric-equatorial RS coincides with the Earth Mean Equator and Equinox of Epoch J2000 (EME2000) and is the one generally used for a 2BP. It constitutes a specific case of the Earth-Centered-Inertial (ECI) RF, where the nutation and libration effects of the planet Earth are taken into account. This fact, strictly speaking, makes the EME2000 RF a quasi-inertial reference system. The choiche to neglect these effects, due to the limitated rotational offset between the two RF, allow us to use the EME2000 RF as an inertial RS. Such RF is presented in Figure 2.1; it's origin is at the Earth's center, the reference plane is the equatorial plane, and its unit vectors $\{\hat{\mathbf{I}}, \hat{\mathbf{J}}, \hat{\mathbf{K}}\}$ have $\hat{\mathbf{I}}$ aligned towards the direction of the Vernal equinox, $\hat{\mathbf{K}}$ normal to the reference plane, and $\hat{\mathbf{J}}$ completing the triad.

For what concerns the satellite motion, on of the most suitable coordinate frames is the perifocal coordinate system [1] . Here the fundamental plane is the plane

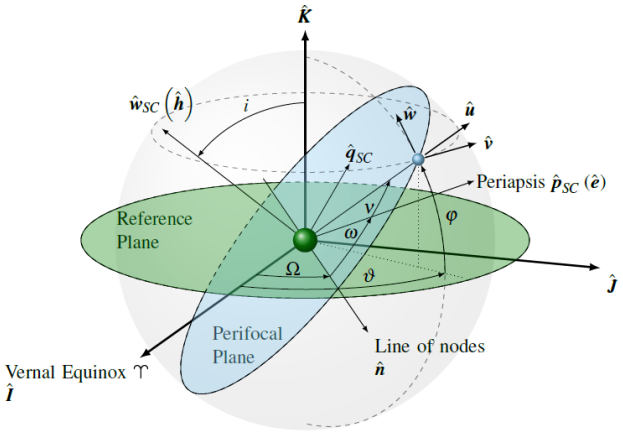

Figure 2.1: EME2000 $\{\hat{\mathbf{I}}, \hat{\mathbf{J}}, \hat{\mathbf{K}}\}$, perifocal $\{\hat{\mathbf{p}}_{SC}, \hat{\mathbf{q}}_{SC}, \hat{\mathbf{w}}_{SC}\}$, and ZEN $\{\hat{\mathbf{u}}, \hat{\mathbf{v}}, \hat{\mathbf{w}}\}$ RSs

of the satellite's orbit and its origin is centered in the gravitational body. It's unit vectors are $\{\hat{\mathbf{p}}_{SC}, \hat{\mathbf{q}}_{SC}, \hat{\mathbf{w}}_{SC}\}$, where the $\hat{\mathbf{p}}_{SC}$ unit vector coincides with the eccentricity vector direction $\hat{\mathbf{e}}$, $\hat{\mathbf{w}}_{SC}$ is normal to the orbital plane and lies in the direction of the specific angular momentum vector $\hat{\mathbf{h}}$, and $\hat{\mathbf{q}}_{SC}$ completes the triad.

According to Kepler's First Law, in this RF a SC moves along a conic as long as it is not afflicted by external perturbations. Five quantities are needed to describe the size, shape and orientation of an orbit, and a sixth element is required to locate the position of the satellite along the orbit at a specific time [15]. These are the "orbital elements": a, e, i, Ω, ω, ν. It is possible to draw the orbit within the perifocal reference system using the semi-major axis a, and the eccentricity e, via the conic equation:

$$r = \frac{a\,(1 - e^2)}{1 + e\cos(\nu)} \tag{2.1}$$

The semi-major axis and the eccentricity are respectively connected to the size and shape of the orbit. The true anomaly ν, is the angular position of SC with respect to the periapsis in the perifocal RF. The other three Keplerian elements are needed to orient the perifocal RF in the tridimensional space with respect to J2000. The inclination i, is the angle between the equatorial and orbit planes, and the intersection between them is called line of nodes $\hat{\mathbf{n}}$. The right ascension of ascending node (RAAN) Ω, is the angle between $\hat{\mathbf{I}}$ and $\hat{\mathbf{n}}$. The argument of the periapsis w, quantifies the angle between the line of nodes and the periapsis, for non-circular orbits.

The Zenith-East-North (ZEN) is a non-inertial RF centered in the SC's center of mass. The choice of the triad $\{\hat{\mathbf{u}}, \hat{\mathbf{v}}, \hat{\mathbf{w}}\}$ allows one to easily describe the SC's velocity components in the radial, tangential, and normal directions, respectively. Once the position vector of the SC from Earth's center has been identified, the radial direction is obtained by extending it. The tangential and normal directions follow the directions of a parallel and a meridian of the celestial sphere.

2.2 Time-invariant coordinate transformation

Several reference systems are used to perform this analysis , and with these the need to transform the vectors from one basis to another arises. This is achieved through elementary rotation matrices, composed of a series of Direction Cosine Matrices (DCMs). For a generic positive rotation of θ, the DCMs are defined in this form:

$$R_1 = \begin{bmatrix} 1 & 0 & 0 \\ 0 & c(\theta) & s(\theta) \\ 0 & -s(\theta) & c(\theta) \end{bmatrix} \quad R_2 = \begin{bmatrix} c(\theta) & 0 & s(\theta) \\ 0 & 1 & 0 \\ -s(\theta) & 0 & c(\theta) \end{bmatrix} \quad R_3 = \begin{bmatrix} c(\theta) & s(\theta) & 0 \\ -s(\theta) & c(\theta) & 0 \\ 0 & 0 & 1 \end{bmatrix}$$

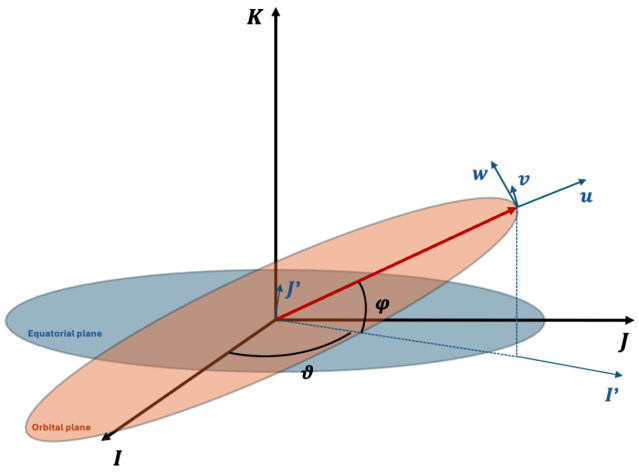

Figure 2.2: Coordinates transformation from J2000 RF to ZEN RF

The transformation of a vector in the $\{\hat{\mathbf{I}}, \hat{\mathbf{J}}, \hat{\mathbf{K}}\}$ basis into a vector expressed in the $\{\hat{\mathbf{u}}, \hat{\mathbf{v}}, \hat{\mathbf{w}}\}$ basis, conceptually corresponds in aligning the two RFs. In the following, it is shown how to realize this transformation through a series of geometrical rotations. The first step is to perform a rotation of θ about the $\hat{\mathbf{K}}$ axis:

$$\mathbf{r}_{\hat{\mathbf{I}}',\hat{\mathbf{J}}',\hat{\mathbf{K}}} = \mathbf{R_3}(\theta)\mathbf{r}_{\hat{\mathbf{I}},\hat{\mathbf{J}},\hat{\mathbf{K}}} \tag{2.2}$$

A second rotation of ϕ about the $\hat{\mathbf{J}}'$ axis allows to make the two frames coincident:

$$\mathbf{r}_{\hat{\mathbf{u}},\hat{\mathbf{v}},\hat{\mathbf{w}}} = \mathbf{R_2}(\phi)\mathbf{r}_{\hat{\mathbf{I}}',\hat{\mathbf{J}}',\hat{\mathbf{K}}} \tag{2.3}$$

If we group the two rotation matrices R_3 and R_2, we can achieve the transformation in a single step:

$$\mathbf{R}_{32}(\theta,\phi) = \mathbf{R_2}(\phi)\mathbf{R_3}(\theta) \tag{2.4}$$

$$\mathbf{r}_{\hat{\mathbf{u}},\hat{\mathbf{v}},\hat{\mathbf{w}}} = \mathbf{R}_{32}(\theta,\phi)\mathbf{r}_{\hat{\mathbf{I}},\hat{\mathbf{J}},\hat{\mathbf{K}}} \tag{2.5}$$

2.3 Two body problem

The dynamic model within which the simulation takes place is a particular case of the N-body problem, where only two bodies are involved. The dominant force acting on bodies in LEO is the Earth's gravity, due to the relatively small distance that separates them. The gravitational effects of the other celestial bodies like the Sun, the Moon and the other planets of the Solar System have a smaller magnitude and are therefore neglected. The two-body problem (2BP) is therefore a good approximation of the motion of two mutually attracting objects according to Newton's law of universal gravitation. It rests on two assumptions:

1. The bodies are spherically symmetric and their masses are concentrated at their centers.
2. The system is subjected to the only gravitational forces that act along the line joining the centers of the two bodies.

Moreover, adopting an inertial coordinate system facilitates the derivation of the following two-body equation, under the assumption that the mass of the smaller body is negligible with respect to that of the larger one:

$$\ddot{\mathbf{r}} = -\frac{\mu}{r^2}\frac{\mathbf{r}}{r} \tag{2.6}$$

These assumptions ensure that certain quantities characterizing the system remain constant; these are known as invariants of motion. The conservation of specific angular momentum:

$$\mathbf{h} = \mathbf{r} \times \mathbf{v} = cost \tag{2.7}$$

confines the spacecraft within a planar orbit. As a consequence, the spacecraft moves faster in the points of the orbit characterized by a small radius, with its

maximum in the periapsis. The opposite happens close to apoapsis. The two terms that make up the specific mechanical energy behave in the same way as the two terms of $\mathbf{h}$: as one increases, the other decreases, so that their sum remains constant. These terms are the specific kinetic energy and the specific potential energy:

$$\mathcal{E} = \frac{V^2}{2} - \frac{\mu}{r} = c \tag{2.8}$$

where c is a constant with an arbitrary value. The vis-viva equation enables the definition of the shape of an orbit through the value of $\mathcal{E}$. Negative values indicate that the orbit is a closed conic section, which can be circular or elliptical, whereas a zero specific mechanical energy results in a parabolic trajectory. Positive values correspond to open orbits with a hyperbolic shape.

2.3.1 Two-body problem governing equations

The following differential equations describe the time evolution of a satellite's state in an inertial reference frame centered on the primary body, e.g., J2000:

$$\frac{d\mathbf{r}}{dt} = \mathbf{V} \tag{2.9}$$

$$\frac{d\mathbf{V}}{dt} = \mathbf{g} + \frac{\mathbf{T}}{m} + \mathbf{a}_p \tag{2.10}$$

$$\frac{dm}{dt} = -\frac{\mathbf{T}}{c} \tag{2.11}$$

Equations (2.9) and (2.10) illustrate how the various contributions influence the spacecraft's acceleration and position. Besides the thrust $\mathbf{T}$, the model also accounts for potential external perturbations $\mathbf{a}_p$. Equation (2.11) gives the fuel mass rate as a function of the thrust and the propulsion system's effective exhaust velocity c.

In the 2BP model, analytical integration is possible only when the satellite is influenced solely by the central gravitational force of the primary body $\mathbf{g}$, without thrust or external perturbations:

$$\mathbf{g} = -\frac{\mu}{r^2}\frac{\mathbf{r}}{r} \tag{2.12}$$

with μ being the gravitational parameter of the central body, and $\mathbf{r}$ the vector pointing from the central body's center of mass to that of the satellite. Under these conditions, the equations of motion reduce to the classical 2BP ODEs, which can

be solved explicitly using Kepler's laws to obtain the position and velocity of the satellite over time.

2.4 Perturbing forces and perturbed satellite orbits

The motion of a satellite around the Earth, or of a spacecraft around the Sun, is governed primarily by the gravitational field of the central body. A radially symmetric mass distribution leads to a conic trajectory, known as a Keplerian orbit. In practice, however, celestial bodies are not perfectly symmetric, and spacecraft are also subject to additional forces. For example, many satellites orbiting the Earth at low altitudes experience a significant influence from the atmosphere. In addition, they are affected by other perturbing forces, such as the gravitational attraction of other celestial bodies — in particular the Sun and the Moon — radiation pressure due to direct sunlight, Earth-reflected sunlight (albedo), Earth's infrared emission, and electromagnetic forces. These perturbations, including those arising from the non-spherical components of the gravitational field, cause deviations from the ideal Keplerian trajectory. Such deviations are generally small, confirming that Keplerian orbits provide a valid and widely used approximation of the actual motion of satellites and spacecraft. These additional forces are called perturbing forces, and the resulting trajectories are referred to as perturbed Keplerian orbits. The choice of which perturbations to include in orbit determination depends on the level of accuracy required for the computed trajectory [16]. The model accounts for atmospheric drag in this analysis:

$$\mathbf{a}_p = \mathbf{a}_{DRAG} \tag{2.13}$$

This perturbation is discussed in detail in the following section.

2.4.1 Atmospheric drag

The different layers of the Earth's atmosphere become increasingly rarefied with altitude. Up to about 1000 km, i.e., throughout the entire LEO region, atmospheric particles are still present and can collide with the satellite, reducing its momentum. In the 600–1000 km range, atmospheric drag can generally be neglected when the mission duration does not exceed a certain threshold. Below 600 km, however—namely at the altitude of interest for the present simulation—a detailed analysis of the satellite's state must necessarily account for this perturbation. In analogy with common practice in aeronautics, the acceleration of a satellite due to atmospheric drag is [16] :

$$\mathbf{a_D} = -\frac{1}{2}\rho\frac{C_D A}{m}v_{rel}^2\frac{\boldsymbol{v}_{rel}}{\|\boldsymbol{v}_{rel}\|} \tag{2.14}$$

where, ρ is the atmospheric density, $\boldsymbol{v}_{rel}$ is the velocity of the satellite relative to the Earth's atmosphere, m is the mass of the satellite and C_D is the drag coefficient related to a reference surface A. The term $\frac{C_D A}{m}$ is referred to as the ballistic coefficient and quantifies the satellite's susceptibility to atmospheric drag. In general, the motion through the upper atmosphere will also generate a force component perpendicular to the velocity vector. In most cases, this component is small when compared to the drag component and we will therefore neglect it [16]. The mass of the satellite is precisely known. Furthermore, if certain assumptions are introduced about atmospheric rotation and about the speed and direction of high-altitude horizontal winds, it becomes possible to determine the velocity of the satellite relative to the atmosphere:

$$\boldsymbol{v}_{rel,IJK} = \boldsymbol{v}_{SC,IJK} - \vec{\omega}_{\oplus} \cdot \mathbf{r}_{IJK} \tag{2.15}$$

The drag coefficient mainly depends on the type of atmospheric particles colliding with the satellite, their kinetic energy, the satellite's velocity, as well as the nature and properties of its surface and its surface temperature. By accounting for all these factors, the drag coefficient can, in principle, be computed for different satellite geometries. Typically, values of C_D range between 2 and 3, with lower altitudes yielding values closer to 2 and higher altitudes tending toward 3. The atmospheric density is obtained from a predefined data set derived from an empirical atmospheric model, providing estimates of the neutral atmosphere from the ground up to approximately 1000 km in altitude.

2.4.2 Validation of the Atmospheric Drag Model

The implemented atmospheric drag model was validated through a numerical propagation starting from an initial circular orbit at an altitude of 200 km. The simulation employed the U.S. Standard Atmosphere 1976 density profile (extracted from PDAS Table 1) and the dynamic formulation described in Section 2.4.1. The spacecraft was characterized by a drag coefficient $C_D = 2.2$, a cross-sectional area $A = 1$ m^2, and a mass $m = 500$ kg, corresponding to a ballistic coefficient $C_D A/m = 4.4 \times 10^{-3}$ m^2/kg.

The propagation results, summarized in Table 2.1, show a progressive decay of altitude that accelerates with time, as expected for drag-dominated low-Earth orbits. During the first 50 revolutions, the altitude decreases almost linearly, with an average loss of about 0.3 km per orbit. After approximately 80 orbits, the effect of atmospheric density growth becomes dominant, and the descent rate increases

exponentially. Re-entry occurs after roughly 91 orbits, corresponding to a few days of orbital lifetime, in excellent agreement with physical expectations and literature data for comparable ballistic coefficients.

The exponential-like behavior of the final decay phase confirms the correct coupling between the drag model and the atmospheric density interpolation, thus validating the implemented approach.

Table 2.1: Altitude decay during propagation starting from 200 km.

Revolutions	**Final Altitude [km]**	Δh **[km]**	**Mean Loss [km/orbit]**
0	200.000	0.000	–
10	197.194	-2.806	-0.281
20	194.099	-5.901	-0.295
30	190.629	-9.371	-0.312
50	182.042	-17.958	-0.359
80	158.206	-41.794	-0.522
90	129.036	-70.964	-0.788
91	110.057	-89.943	-0.989
91.1	103.083	-96.917	-0.983
91.2	85.739	-114.261	-0.950
91.25	43.911	-156.089	-1.710
91.28	8.946	-191.054	-6.820
91.3	0.754	-199.246	-6.640

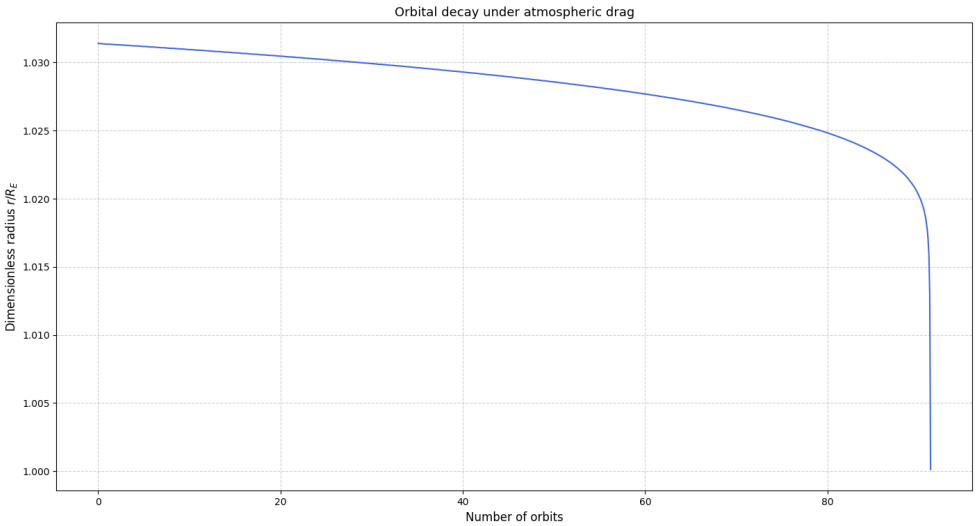

Figure 2.3: Orbital decay under atmospheric drag

Chapter 3

Optimal Control Theory

Maximizing the effectiveness of a space mission requires the efficient use of every available resource. In the design phase, not only the total mass of the satellite is a critical parameter, but also its distribution among the various systems. Optimizing the mass allocation across subsystems increases flexibility in payload selection, ultimately enhancing the scientific return of the mission. This consideration applies to all satellite systems and subsystems, including the fuel stored on board.

A satellite can move from an initial to a final state through multiple possible trajectories. Among these, the one that consumes the least fuel while satisfying all boundary conditions is the optimal solution. Optimal Control Theory (OCT) provides the framework to identify such solutions by defining the conditions that distinguish them from suboptimal ones. An Optimal Control Problem (OCP) seeks the control law that extremizes a chosen performance index. In this thesis, the index is the satellite's final mass—equivalent to minimizing the propellant required for the transfer. The term "optimal control law" refers to the set of control variables that govern the mission's evolution. The objective is to regulate these variables so as to meet all constraints while maximizing the chosen index of merit.

3.1 Introduction to direct, indirect, and genetic algorithm approaches

Numerical methods can be broadly divided into two main categories: direct and indirect. Both aim at transforming a complex problem into a sequence of smaller and more tractable subproblems. The scientific community has employed both approaches successfully, particularly in the context of trajectory optimization for space missions. Continuous comparison between the two has made it possible to clearly identify their respective strengths and weaknesses. More recently, a third

class of methods — Genetic Algorithms (GAs) — has also gained attention. A brief overview of this approach will be provided in the final part of this section.

In recent years, direct numerical methods have been more widely adopted. These approaches approximate a generic time-continuous problem by discretizing the state and control variables. The accuracy of the resulting solution improves as the discretization grid becomes finer. This was once a limiting factor, but the advent of modern computers, with their increased computational power, has made it feasible to handle problems of this scale. The main drawback of this approach lies in the limited accuracy of the solutions, even with very fine discretization meshes, making post-processing or refinement techniques necessary. Another important limitation is that direct methods provide little theoretical insight: it is difficult to assess whether a solution is truly optimal, or how far it lies from the optimum.

Solutions obtained through indirect methods are undeniably more accurate and require lower computational cost; however, achieving convergence is considerably more challenging. This difficulty arises from the need to select a set of problem-dependent parameters that must be derived from OCT. Convergence to the solution is highly sensitive to the choice of initial conditions, making it necessary for the user to develop a certain familiarity with the specific problem. On the other hand, indirect methods provide a wealth of theoretical information that enables the assessment of solution optimality. Even when the obtained solution is not optimal, these theoretical insights remain available and can be exploited to improve the result [1].

Alongside direct and indirect methods, genetic algorithms (GAs) provide a heuristic alternative, drawing inspiration from the mechanisms of natural evolution. They operate by evolving a population of candidate solutions through iterative processes of selection, crossover, and mutation, progressively converging toward improved solutions. Unlike direct and indirect methods, GAs do not require gradient information or an explicit formulation of the necessary optimality conditions, which makes them particularly suitable for highly nonlinear or discontinuous problems. However, this flexibility comes at the cost of higher computational effort and the absence of guarantees regarding convergence to the global optimum. Finite-thrust mission optimization is best modeled within the framework of a continuous-time optimal control problem [18].

3.2 Fundamentals of optimal control theory

Optimal Control Theory (OCT) provides a mathematical framework for determining the control laws that optimize the behavior of dynamical systems subject to physical or operational constraints. Originating from the calculus of variations, OCT extends

its principles to systems described by differential equations, where the objective is to identify control inputs that maximize or minimize a given performance measure. This framework has found extensive applications in aerospace engineering, robotics, and economics, among other fields, due to its ability to handle both dynamic and boundary constraints in a unified manner.

Within this theoretical context, an *Optimal Control Problem* (OCP) seeks to determine an admissible control law that maximizes (or minimizes) a chosen performance index, while ensuring that the dynamical system satisfies all prescribed constraints as it evolves from an initial to a final state over a specified time interval.

The system dynamics are described by a set of n first-order differential equations involving the state vector $\mathbf{x}(t) \in \mathbb{R}^n$ and the control vector $\mathbf{u}(t) \in \mathbb{R}^m$, where m denotes the number of control variables. The system can therefore be expressed as:

$$\dot{\mathbf{x}}(t) = \mathbf{f}\Big(\mathbf{x}(t), \mathbf{u}(t), t\Big) \tag{3.1}$$

The optimal solution of the problem defines the trajectory $\mathbf{x}^*(t)$ and the corresponding control $\mathbf{u}^*(t)$ that optimize the selected merit index, while satisfying all system and boundary constraints. When these constraints involve only the values of the state and time variables at the beginning and at the end of the time interval, the problem of Eq. (3.1) becomes a *Two-Point Boundary Value Problem* (TPBVP). The boundary conditions imposed at $t = t_0$ and $t = t_f$ are referred to as *external boundaries*, and can be expressed as a set of homogeneous algebraic equations:

$$\boldsymbol{\chi}(\mathbf{x}_0, \mathbf{x}_f, t_0, t_f) = 0 \tag{3.2}$$

where $\boldsymbol{\chi} : [\mathbb{R}^n, \mathbb{R}^n, \mathbb{R}, \mathbb{R}] \to \mathbb{R}^q$ collects the q boundary constraints, and $\mathbf{x}_0$ and $\mathbf{x}_f$ denote $\mathbf{x}(t_0)$ and $\mathbf{x}(t_f)$, respectively.

In addition to boundary conditions, constraints may also be imposed directly on the control variables, so that $\mathbf{u}(t) \in \mathcal{U}$, where $\mathcal{U}$ represents the set of admissible controls.

The quantity that drives the optimization process is the *performance index* (or cost functional) J, which is to be either maximized or minimized. In its most general form, J can be expressed as:

$$J = \varphi(\mathbf{x}_0, \mathbf{x}_f, t_0, t_f) + \int_{t_0}^{t_f} \Phi(\mathbf{x}(t), \mathbf{u}(t), t)\, dt \tag{3.3}$$

where:

- φ depends solely on the boundary values of the state and time variables, quantifying the cost associated with reaching the desired final state;
- the integral term accounts for the contributions accumulated along the trajectory, representing the overall performance of the system throughout its evolution.

Equation (3.3) is known as the *Bolza formulation* of the optimal control problem. Depending on the choice of φ and Φ, the problem can also be expressed in the *Lagrange* form (by setting $\varphi = 0$) or in the *Mayer* form (by setting $\Phi = 0$ and introducing auxiliary variables). The Mayer formulation is typically preferred for numerical optimization, as it allows the cost functional to be expressed explicitly in terms of the boundary variables only—an approach adopted in this work.

The general structure of the Bolza problem can therefore be summarized as:

$$P_{\text{Bolza}} = \begin{cases} \text{maximize} \quad J = \varphi(\mathbf{x}_0, \mathbf{x}_f, t_0, t_f) \\ \text{subject to:} \\ \dot{\mathbf{x}}(t) = \mathbf{f}(\mathbf{x}(t), \mathbf{u}(t), t) \\ \boldsymbol{\chi}(\mathbf{x}_0, \mathbf{x}_f, t_0, t_f) = 0 \end{cases} \tag{3.4}$$

A minimization problem can be obtained equivalently by changing the sign of φ. In the present work, the OCP is formulated as a maximization problem.

A key step in deriving the necessary conditions for optimality consists in introducing the principles of the *Indirect Method* (IM). This is achieved through the definition of an *augmented performance index*, denoted as J^*, which incorporates a measure of how accurately the state dynamics and boundary constraints are satisfied.

To accomplish this, two additional sets of variables are introduced:

- the *adjoint variables*, collected in the vector $\boldsymbol{\lambda}(t)$, associated with the state variables $\mathbf{x}(t)$;
- the *Lagrange multipliers*, gathered in the vector $\boldsymbol{\mu}$, associated with the boundary conditions.

Hence, one has $\boldsymbol{\lambda} \in \mathbb{R}^n$ and $\boldsymbol{\mu} \in \mathbb{R}^m$. The augmented performance index can therefore be written as:

$$J^* = \varphi + \boldsymbol{\mu}^T \boldsymbol{\chi} + \int_{t_0}^{t_f} \left[\Phi + \boldsymbol{\lambda}^T (\mathbf{f} - \dot{\mathbf{x}}) \right] dt \tag{3.5}$$

where the following notation has been introduced for brevity:

$$\varphi \triangleq \varphi(\mathbf{x}_0, \mathbf{x}_f, t_0, t_f) \tag{3.6}$$

$$\boldsymbol{\chi} \triangleq \boldsymbol{\chi}(\mathbf{x}_0, \mathbf{x}_f, t_0, t_f) \tag{3.7}$$

Both the original and augmented performance indices depend on the state variables $\mathbf{x}(t)$, their time derivatives $\dot{\mathbf{x}}(t)$, and the control variables $\mathbf{u}(t)$. For a non-converged trajectory, when the boundary conditions are not satisfied ($\boldsymbol{\chi} \neq 0$) or the dynamic model is not respected ($\dot{\mathbf{x}} \neq \mathbf{f}$), the two functionals differ. Conversely,

if both constraints are fulfilled — i.e., $\boldsymbol{\chi} = 0$ and $\dot{\mathbf{x}} = \mathbf{f}$ — then $J = J^*$. Thus, solving the augmented problem is *mathematically equivalent* to solving the original one, provided that all constraints are enforced.

During the trajectory optimization process, the state derivatives $\dot{\mathbf{x}}$ are integrated numerically and are not explicitly known. It is therefore convenient to eliminate their dependence by integrating the term $-\boldsymbol{\lambda}^T\dot{\mathbf{x}}$ by parts:

$$\int_{t_0}^{t_f} \left(-\boldsymbol{\lambda}^T\dot{\mathbf{x}}\right) dt = -\boldsymbol{\lambda}_f^T\mathbf{x}_f + \boldsymbol{\lambda}_0^T\mathbf{x}_0 + \int_{t_0}^{t_f} \dot{\boldsymbol{\lambda}}^T\mathbf{x}\, dt \tag{3.8}$$

Substituting Equation (3.8) into Equation (3.5) yields:

$$J^* = \varphi + \boldsymbol{\mu}^T\boldsymbol{\chi} + \left(\boldsymbol{\lambda}_0^T\mathbf{x}_0 - \boldsymbol{\lambda}_f^T\mathbf{x}_f\right) + \int_{t_0}^{t_f} \left[\Phi + \boldsymbol{\lambda}^T\mathbf{f} - \dot{\boldsymbol{\lambda}}^T\mathbf{x}\right] dt \tag{3.9}$$

At this point, a useful quantity naturally arises — the *Hamiltonian function* of the system, defined as:

$$H \triangleq \Phi + \boldsymbol{\lambda}^T\mathbf{f} \tag{3.10}$$

The necessary conditions for optimality require the first variation of the augmented index to vanish, i.e. $\delta J^* = 0$. After standard manipulations, one obtains:

$$\delta J^* = \left(\frac{\partial\varphi}{\partial t_0} + \boldsymbol{\mu}^T\frac{\partial\boldsymbol{\chi}}{\partial t_0} - H_0\right)\delta t_0 \tag{3.11a}$$

$$+ \left(\frac{\partial\varphi}{\partial t_f} + \boldsymbol{\mu}^T\frac{\partial\boldsymbol{\chi}}{\partial t_f} + H_f\right)\delta t_f \tag{3.11b}$$

$$+ \left(\frac{\partial\varphi}{\partial\mathbf{x}_0} + \boldsymbol{\mu}^T\frac{\partial\boldsymbol{\chi}}{\partial\mathbf{x}_0} + \boldsymbol{\lambda}_0^T\right)\delta\mathbf{x}_0 \tag{3.11c}$$

$$+ \left(\frac{\partial\varphi}{\partial\mathbf{x}_f} + \boldsymbol{\mu}^T\frac{\partial\boldsymbol{\chi}}{\partial\mathbf{x}_f} - \boldsymbol{\lambda}_f^T\right)\delta\mathbf{x}_f \tag{3.11d}$$

$$+ \int_{t_0}^{t_f} \left[\left(\frac{\partial H}{\partial\mathbf{x}} + \dot{\boldsymbol{\lambda}}^T\right)\delta\mathbf{x} + \frac{\partial H}{\partial\mathbf{u}}\,\delta\mathbf{u}\right] dt \tag{3.11e}$$

By suitably defining the adjoint variables $\boldsymbol{\lambda}(t)$ and multipliers $\boldsymbol{\mu}$, one can make $\delta J^* = 0$ for arbitrary variations δt_0, δt_f, $\delta\mathbf{x}_0$, $\delta\mathbf{x}_f$, $\delta\mathbf{x}$, and $\delta\mathbf{u}$. The vanishing of the coefficients multiplying each variation leads to a complete set of *necessary conditions for optimality*:

- the coefficients of δt_0 and δt_f yield the *transversality conditions*;

- the coefficients of $\delta\mathbf{x}_0$ and $\delta\mathbf{x}_f$ yield $2n$ algebraic *boundary optimality conditions*;

- the remaining coefficients provide n *Euler–Lagrange differential equations* for the adjoint variables and m algebraic equations defining the optimal control.

3.2.1 Boundary conditions for optimality

The boundary conditions associated with the optimality of an Optimal Control Problem arise from the requirement that the first-order variation of the augmented merit function be null for any admissible perturbation of time and state variables. By imposing that the coefficients multiplying δt_0, δt_f, $\delta\mathbf{x}_0$, and $\delta\mathbf{x}_f$ in Eq. (3.11) vanish, one obtains the following set of algebraic relations:

$$\frac{\partial\varphi}{\partial t_0} + \boldsymbol{\mu}^T\frac{\partial\boldsymbol{\chi}}{\partial t_0} - H_0 = 0, \tag{3.12a}$$

$$\frac{\partial\varphi}{\partial t_f} + \boldsymbol{\mu}^T\frac{\partial\boldsymbol{\chi}}{\partial t_f} + H_f = 0, \tag{3.12b}$$

$$\frac{\partial\varphi}{\partial\mathbf{x}_0} + \boldsymbol{\mu}^T\frac{\partial\boldsymbol{\chi}}{\partial\mathbf{x}_0} - \boldsymbol{\lambda}_0^T = 0, \tag{3.12c}$$

$$\frac{\partial\varphi}{\partial\mathbf{x}_f} + \boldsymbol{\mu}^T\frac{\partial\boldsymbol{\chi}}{\partial\mathbf{x}_f} + \boldsymbol{\lambda}_f^T = 0. \tag{3.12d}$$

Equations (3.12a)–(3.12b) represent the *transversality conditions* and describe how the initial and final times must behave in order to ensure optimality. If the time variable does not explicitly appear in the function φ and is not constrained through $\boldsymbol{\chi}$, then the corresponding Hamiltonian must vanish at that point, i.e. $H_0 = H_f = 0$. In this case, both t_0 and t_f are free and their values are determined through the optimization process. Conversely, when time is constrained — for instance, if $\boldsymbol{\chi}$ includes relations such as $t_0 = a$ and/or $t_f = b$ — the Hamiltonian at that boundary is free to assume any value. An illustrative case is that of a mission with a fixed duration Δt, for which both the initial epoch t_0 and the final epoch $t_f = t_0 + \Delta t$ are imposed; consequently, $H_0 \neq 0$ and $H_f \neq 0$. In contrast, for problems with a free final time, t_0 is fixed while t_f is unbounded and subject to optimization, thus implying $H_0 \neq 0$ and $H_f = 0$.

The optimality conditions in Eqs. (3.12c)–(3.12d) apply analogously to the state variables. If a given state component x_i does not explicitly appear in the boundary function φ and is not involved in any constraint within $\boldsymbol{\chi}$, its corresponding adjoint variable vanishes at that boundary, i.e. $\lambda_{x_i} = 0$. Conversely, when the value of x_i is prescribed, the associated adjoint variable is free.

3.2.2 Equations for adjoint and control variables

The set of ODEs obtained by setting to zero the coefficients multiplying the variations in the last line (3.11e) of equation (3.11) describes the temporal evolution of both the adjoint variables and the control vector. In particular, by nullifying the coefficient of $\delta\mathbf{x}$, one obtains the Euler–Lagrange equations governing the adjoint variables:

$$\dot{\boldsymbol{\lambda}} = -\left(\frac{\partial \mathcal{H}}{\partial \mathbf{x}}\right)^T, \tag{3.13}$$

where $\boldsymbol{\lambda} \in \mathbb{R}^n$ represents the vector of adjoint variables, each of which is uniquely associated with a corresponding state variable.

Conversely, by nullifying the coefficient of $\delta\mathbf{u}$, one obtains m algebraic relations that define the optimal control conditions:

$$\left(\frac{\partial \mathcal{H}}{\partial \mathbf{u}}\right)^T = \mathbf{0}. \tag{3.14}$$

In general, one or more components of the control vector $\mathbf{u}$ may be subject to explicit bounds, denoted as $\mathcal{U}$. The control can depend on both the state and time, i.e. $\mathbf{u} = \mathbf{u}(\mathbf{x}(t), t)$, but in this work only explicit admissibility constraints are considered. For instance, a specific control variable u may be constrained within the limits $U_{\min} \leq u \leq U_{\max}$.

When explicit bounds are present, the optimal control $\mathbf{u}^* \in \mathcal{U}$ at any given time instant is the one that extremizes the Hamiltonian $\mathcal{H}$ in equation (3.10). This statement corresponds to the *Pontryagin's Maximum Principle* (PMP) for a maximization problem (or the *Pontryagin's Minimum Principle*, PmP, for minimization problems). The PMP implies that the optimal control may lie either within the admissible interval or on its boundary. Specifically, when $U_{\min} < u < U_{\max}$, the optimal value satisfies equation (3.14); otherwise, it takes one of the boundary values of $\mathcal{U}$.

However, equation (3.14) cannot be satisfied if the Hamiltonian is linear (or affine) with respect to the control variable. In such a case, the following condition arises:

$$\frac{\partial \mathcal{H}}{\partial u_i} = \begin{cases} k_{u_i}, & \text{if } \mathcal{H} \text{ is affine in } u_i, \\ f(u_i), & \text{otherwise,} \end{cases} \tag{3.15}$$

where k_{u_i} is a constant coefficient.

When $\mathcal{H}$ is affine in u_i, equation (3.15) cannot be fulfilled (except for $k_{u_i} = 0$), since u_i does not appear explicitly in the partial derivative. In this scenario, the optimal strategy depends on the sign of k_{u_i}: if $k_{u_i} > 0$, the Hamiltonian is maximized by setting $u_i = U_{i,\max}$; if $k_{u_i} < 0$, then $u_i = U_{i,\min}$. This type of solution is known as *bang-bang control*.

In the present problem, this is precisely the situation that occurs: the Hamiltonian is linear with respect to the selected control variable — the thrust magnitude T — under specific assumptions that will be detailed later in this work. Moreover, the switching behaviour between the two admissible limits, $T_{\min}$ (typically zero) and $T_{\max}$, plays a crucial role in determining the optimal trajectory.

If $k_{u_i} = 0$ for a finite time interval, the control is said to be in a *singular arc*, and a different optimization strategy must be adopted. Such a case does not occur in the present work and is therefore omitted for brevity.

Finally, once the m boundary conditions $\boldsymbol{\chi} = \mathbf{0}$ are imposed, the problem can be formulated as a two-point boundary value problem (TPBVP) consisting of $2 + 2n + m$ equations. These equations arise respectively from transversality conditions (equations (4.10a)–(4.10b)), optimality conditions (equations (4.10c)–(4.10d)), and control relations (equation (3.14)). They implicitly determine the two time instants (t_0, t_f), the initial conditions for the $2n$ differential equations governing $\mathbf{x}$ and $\boldsymbol{\lambda}$, and the m adjoint constants $\boldsymbol{\mu}$.

3.3 Multi-point optimal control problem

A Multi-Point Boundary Value Problem (MPBVP) arises when additional constraints are imposed at internal points along the trajectory, for instance when a flyby occurs during an interplanetary mission. In such cases, the entire trajectory can be divided into n_p subintervals, referred to as *phases* or *arcs*. This segmentation not only allows the imposition of internal constraints but also enhances numerical robustness and convergence properties.

Each arc is continuous in its state evolution, while discontinuities may occur at the internal boundaries, i.e., at the junctions between adjacent arcs. As a result, the general formulation introduced in equations (3.1)–(3.3) extends naturally to the MPBVP framework.

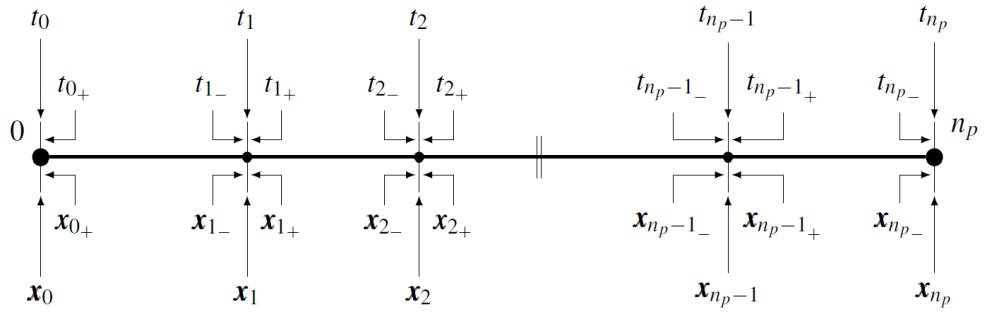

Figure 3.1: Schematic representation of the multi-point boundary value problem with n_p arcs, [1].

Let each j-th arc start at $t^+_{(j-1)}$ and terminate at t^-_j, with corresponding state vectors $\mathbf{x}^+_{(j-1)}$ and $\mathbf{x}^-_j$. For brevity, the notation $\mathbf{x}(t_j) \equiv \mathbf{x}_j$ is introduced. Each j-th arc spans a time interval Δt_j, which is in general unknown and treated as an optimization variable.

The boundary conditions (BCs) for the MPBVP are typically nonlinear and mixed. They can be imposed not only at the external boundaries but also at internal junctions between arcs, and are expressed as:

$$\boldsymbol{\chi}\left(\mathbf{x}^+_{(j-1)}, \mathbf{x}^-_j, t^+_{(j-1)}, t^-_j\right) = \mathbf{0}, \quad j = 1, \ldots, n_p. \tag{3.16}$$

The performance index of the optimal control MPBVP is therefore written as:

$$J = \varphi\left(\mathbf{x}^+_{(j-1)}, \mathbf{x}^-_j, t^+_{(j-1)}, t^-_j\right) + \sum_{j=1}^{n_p} \int_{t^+_{(j-1)}}^{t^-_j} \Phi(\mathbf{x}(t), \mathbf{u}(t), t)\, dt. \tag{3.17}$$

The terminal function φ depends on the boundary values of the state and time variables, while the summation of the integrals of Φ accounts for the evolution of the system along each arc.

The augmented merit index becomes:

$$J^* = \varphi + \boldsymbol{\mu}^T \boldsymbol{\chi} + \sum_{j=1}^{n_p} \int_{t^+_{(j-1)}}^{t^-_j} \left[\Phi + \boldsymbol{\lambda}^T (\mathbf{f} - \dot{\mathbf{x}})\right] dt, \tag{3.18}$$

which, after integrating by parts, becomes:

$$\begin{aligned} J^* = \varphi + \boldsymbol{\mu}^T \boldsymbol{\chi} + \sum_{j=1}^{n_p} \left[\boldsymbol{\lambda}^{+T}_{(j-1)} \mathbf{x}^+_{(j-1)} - \boldsymbol{\lambda}^{-T}_j \mathbf{x}^-_j\right] \\ + \sum_{j=1}^{n_p} \int_{t^+_{(j-1)}}^{t^-_j} \left[\Phi + \boldsymbol{\lambda}^T \mathbf{f} - \dot{\boldsymbol{\lambda}}^T \mathbf{x}\right] dt. \end{aligned} \tag{3.19}$$

The first-order variation δJ^* for each arc can then be expressed as:

$$\delta J^* = \left(\frac{\partial \varphi}{\partial t^+_{(j-1)}} + \boldsymbol{\mu}^T \frac{\partial \boldsymbol{\chi}}{\partial t^+_{(j-1)}} - H^+_{(j-1)} \right) \delta t^+_{(j-1)} \tag{3.20a}$$

$$+ \left(\frac{\partial \varphi}{\partial t^-_j} + \boldsymbol{\mu}^T \frac{\partial \boldsymbol{\chi}}{\partial t^-_j} + H^-_j \right) \delta t^-_j \tag{3.20b}$$

$$+ \left(\frac{\partial \varphi}{\partial \mathbf{x}^+_{(j-1)}} + \boldsymbol{\mu}^T \frac{\partial \boldsymbol{\chi}}{\partial \mathbf{x}^+_{(j-1)}} + \boldsymbol{\lambda}^{+T}_{(j-1)} \right) \delta \mathbf{x}^+_{(j-1)} \tag{3.20c}$$

$$+ \left(\frac{\partial \varphi}{\partial \mathbf{x}^-_j} + \boldsymbol{\mu}^T \frac{\partial \boldsymbol{\chi}}{\partial \mathbf{x}^-_j} - \boldsymbol{\lambda}^{-T}_j \right) \delta \mathbf{x}^-_j \tag{3.20d}$$

$$+ \sum_{j=1}^{n_p} \int_{t^+_{(j-1)}}^{t^-_j} \left[\left(\frac{\partial H}{\partial \mathbf{x}} + \dot{\boldsymbol{\lambda}}^T \right) \delta \mathbf{x} + \frac{\partial H}{\partial \mathbf{u}} \, \delta \mathbf{u} \right] dt, \tag{3.20e}$$

where H denotes the Hamiltonian of the system.

Finally, the optimality and transversality conditions for the MPBVP can be conveniently expressed in terms of the j-th boundary itself:

$$\frac{\partial \varphi}{\partial t^+_j} + \boldsymbol{\mu}^T \frac{\partial \boldsymbol{\chi}}{\partial t^+_j} - H^+_j = 0, \qquad j = 0, \ldots, n_p - 1, \tag{3.21a}$$

$$\frac{\partial \varphi}{\partial t^-_j} + \boldsymbol{\mu}^T \frac{\partial \boldsymbol{\chi}}{\partial t^-_j} + H^-_j = 0, \qquad j = 1, \ldots, n_p, \tag{3.21b}$$

$$\frac{\partial \varphi}{\partial \mathbf{x}^+_j} + \boldsymbol{\mu}^T \frac{\partial \boldsymbol{\chi}}{\partial \mathbf{x}^+_j} + \boldsymbol{\lambda}^{+T}_j = 0, \qquad j = 0, \ldots, n_p - 1, \tag{3.21c}$$

$$\frac{\partial \varphi}{\partial \mathbf{x}^-_j} + \boldsymbol{\mu}^T \frac{\partial \boldsymbol{\chi}}{\partial \mathbf{x}^-_j} - \boldsymbol{\lambda}^{-T}_j = 0, \qquad j = 1, \ldots, n_p. \tag{3.21d}$$

The same considerations previously derived for the Euler–Lagrange equations of the adjoint variables and the control equations remain valid in the MPBVP framework.

3.4 Formulation and single-shooting implementation of the two-point boundary value problem

This section presents the implementation of the Boundary Value Problem (BVP) within the framework of Optimal Control Theory (OCT). The primary objective is to optimise the descent trajectory of a spacecraft operating in Low Earth Orbit

(LEO), subject to the gravitational influence of the central body and modelled within a medium-fidelity Two-Body Problem (2BP). The formulation aims to determine the optimal control history that maximizes the selected performance index while ensuring adherence to the prescribed boundary conditions and system dynamics. The formulation of a BVP in this context requires accurate control and optimization procedures capable of addressing potential numerical challenges that may hinder convergence, due to the inherently nonlinear nature of the system. When adopting an Indirect Method (IM), particular attention must be devoted to the robustness of the numerical scheme and to the sensitivity of the solution with respect to small perturbations in the initial conditions.

To tackle this challenge, a Two-Point Boundary Value Problem (TPBVP) approach is adopted. This formulation is appropriate since OCT increases the dimensionality of the problem compared to the original 2BP, as previously discussed. In this framework, the initial state vector includes both the physical state variables (some of which may be unknown) and their associated adjoint variables:

$$\mathbf{y}_0 = \begin{bmatrix} \mathbf{x}^T & \boldsymbol{\lambda}^T \end{bmatrix}^T \tag{3.22}$$

The goal of the BVP is to determine the optimal initial conditions $\mathbf{y}_0^*$ that yield the desired final state $\mathbf{y}_f^*$, while satisfying all boundary conditions (BCs), including both constrained and optimality-related ones. Among the available strategies, the single-shooting method is preferred for its simplicity and moderate computational requirements. This method iteratively adjusts the initial conditions until the desired terminal constraints are met, as detailed in [1]. Such a procedure aligns with the objective of developing a robust IM-based algorithm for the dynamics of the 2BP.

The general form of the ODE system for the IM can be expressed as:

$$\dot{\mathbf{y}}(t) = \mathbf{f}(\mathbf{y}(t), t) \tag{3.23}$$

Introducing a new vector $\mathbf{z}$ defined as:

$$\mathbf{z} = \begin{bmatrix} \mathbf{y}^T & \mathbf{c}^T \end{bmatrix}^T \tag{3.24}$$

where $\mathbf{c}$ is a constant vector, the system can be rewritten as:

$$\dot{\mathbf{z}} = \mathbf{f}(\mathbf{z}(t), t) \tag{3.25}$$

with

$$\dot{\mathbf{c}} = 0. \tag{3.26}$$

The corresponding boundary conditions, including both imposed and optimal ones, must satisfy:

$$\boldsymbol{\chi}(\mathbf{z}) = 0, \tag{3.27}$$

where $\mathbf{z}$ collects the variable values at the internal and external boundaries.

The purpose of this analysis is to find the optimal initial design vector $\mathbf{q}_0^*$ that leads to the desired final state while satisfying all constraints. This is achieved via a single-shooting procedure, in which the initial guess $\mathbf{q}_r = \mathbf{z}_0$ is iteratively refined. At each iteration r, the boundary condition deviation is denoted as $\boldsymbol{\chi}_r = \boldsymbol{\chi}(\mathbf{q}_r)$. The relationship between successive iterations is approximated using a first-order Taylor expansion:

$$\boldsymbol{\chi}(\mathbf{q}_{r+1}) = \boldsymbol{\chi}(\mathbf{q}_r) + \frac{\partial \boldsymbol{\chi}(\mathbf{q}_r)}{\partial \mathbf{q}_{r+1}}(\mathbf{q}_{r+1} - \mathbf{q}_r) \tag{3.28}$$

If a solution exists such that $\boldsymbol{\chi}_{r+1} = 0$, the iterative correction can be expressed as:

$$\boldsymbol{\chi}_r + [\mathcal{J}(\boldsymbol{\chi}_r)](\mathbf{q}_{r+1} - \mathbf{q}_r) = 0 \tag{3.29}$$

where $\mathcal{J}(\boldsymbol{\chi}_r)$ is the Jacobian matrix of the constraint vector. Hence, the design vector is updated according to:

$$\mathbf{q}_{r+1} = \mathbf{q}_r - [\mathcal{J}(\boldsymbol{\chi}_r)]^{-1}\boldsymbol{\chi}_r \tag{3.30}$$

The Jacobian matrix is computed through a forward finite difference scheme:

$$\mathcal{J}(\boldsymbol{\chi}_r) = \frac{\boldsymbol{\chi}_r^p - \boldsymbol{\chi}_r}{\Delta} \tag{3.31}$$

where $\boldsymbol{\chi}_r^p = \boldsymbol{\chi}(\mathbf{q}_r^p)$ represents the constraint vector obtained after perturbing the variable vector by a small increment $\Delta = 10^{-7}$:

$$\boldsymbol{\chi}_r^p \equiv \boldsymbol{\chi}(\mathbf{q}_r^p) \tag{3.32a}$$

$$\mathbf{q}_r^p \equiv \mathbf{q}_r + \Delta \tag{3.32b}$$

Although this approach introduces a certain approximation, it greatly improves the stability of the algorithm against perturbations in the initial guess.

The resulting Optimal Control Problem (OCP) within the TPBVP framework thus seeks the optimal initial state $\mathbf{z}_0^*$ that drives the system to the desired final state $\mathbf{z}_f^*(t)$ while fulfilling all boundary conditions. This is achieved through the simultaneous integration of the system of ODEs and the associated State Transition Matrix (STM) equations:

$$\dot{\mathbf{z}} = \mathbf{f}(\mathbf{z}(t), t) \tag{3.33}$$

In practice, the iterative Differential Corrector (DC) process based on the STM can introduce numerical errors that may compromise convergence. To mitigate

this, two stabilization strategies are employed. First, a relaxation parameter κ_1 is introduced in the correction equation to enhance convergence:

$$\mathbf{z}_{r+1} = \mathbf{z}_r - \kappa_1 \left[\mathcal{J}(\boldsymbol{\chi}_r)\right]^{-1} \boldsymbol{\chi}_r \tag{3.34}$$

where κ_1 ranges between 0.1 and 1. Lower values are typically used during the early iterations (to ensure stability), whereas higher values are preferable once the solution approaches convergence.

Second, the maximum boundary condition error, defined as $E_{\max} = \max_i(\|\chi_i\|)$, is monitored across iterations according to:

$$E_{\max,r+1} < \kappa_2 \, E_{\max,r} \tag{3.35}$$

with κ_2 typically between 2 and 3. If the inequality in Eq. (3.35) is not satisfied, the relaxation factor κ_1 is reduced to restore convergence.

3.5 OCP for LEO Descent Trajectory Optimization

The present section illustrates the application of the Optimal Control Theory (OCT) to the selected case study. The adopted objective consists in the *maximization of the final mass*, which is equivalent to the *minimization of the propellant consumption*. This goal can be expressed through a merit index, which depends on the control law vector $\vec{u} = \vec{T}$ and on the following state vector:

$$\vec{x} = \{r, \vartheta, \phi, u, v, w, m\}^T \tag{3.36}$$

where $\vec{x} \in \mathbb{R}^n$. Each of these state variables is associated with a corresponding adjoint, or *costate*, variable, forming together the augmented vector $\vec{y} \in \mathbb{R}^{2n}$ defined as:

$$\vec{y} = \{r, \vartheta, \phi, u, v, w, m, \lambda_r, \lambda_\vartheta, \lambda_\phi, \lambda_u, \lambda_v, \lambda_w, \lambda_m\}^T \tag{3.37}$$

The equations governing the satellite's dynamics can be expressed through the following system of ordinary differential equations:

$$\begin{cases} \dfrac{dr}{dt} = u \\ \dfrac{d\vartheta}{dt} = \dfrac{v}{r\cos\phi} \\ \dfrac{d\phi}{dt} = \dfrac{w}{r} \\ \dfrac{du}{dt} = -\dfrac{\mu}{r^2} + \dfrac{v^2}{r} + \dfrac{w^2}{r} + \dfrac{T_u}{m} + (a_p)_u \\ \dfrac{dv}{dt} = -\dfrac{uv}{r} + \dfrac{vw}{r}\tan\phi + \dfrac{T_v}{m} + (a_p)_v \\ \dfrac{dw}{dt} = -\dfrac{uw}{r} - \dfrac{v^2}{r}\tan\phi + \dfrac{T_w}{m} + (a_p)_w \\ \dfrac{dm}{dt} = -\dfrac{T}{c} \end{cases} \tag{3.38}$$

From this system, the Hamiltonian function can be formulated as:

$$H = \vec{\lambda}^T \vec{f} = \sum_{i=1}^{2n} \lambda_i f_i \tag{3.39}$$

Once expanded, and highlighting the terms depending on the thrust magnitude T, the Hamiltonian becomes:

$$\begin{aligned} H = {} & \lambda_r u + \lambda_\vartheta \frac{v}{r\cos\phi} + \lambda_\phi \frac{w}{r} + \lambda_u \left(-\frac{\mu}{r^2} + \frac{v^2}{r} + \frac{w^2}{r} + (a_p)_u \right) \\ & + \lambda_v \left(-\frac{uv}{r} + \frac{wv}{r}\tan\phi + (a_p)_v \right) + \lambda_w \left(-\frac{uw}{r} - \frac{v^2}{r}\tan\phi + (a_p)_w \right) \\ & + \frac{T}{m} \left(\vec{\lambda}_V^T \frac{\vec{T}}{T} - \lambda_m \frac{m}{c} \right), \end{aligned} \tag{3.40}$$

where $\vec{\lambda}_V$ is known as the *primer vector*, defined as $\lambda_V = \sqrt{\lambda_u^2 + \lambda_v^2 + \lambda_w^2}$. From this expression, the so-called *switching function* can be derived as:

$$SF = \vec{\lambda}_V^T \frac{\vec{T}}{T} - \lambda_m \frac{m}{c} \tag{3.41}$$

According to the *bang–bang* control theory (see Section 3.2.2), the optimal thrust magnitude can then be obtained as:

$$T = \begin{cases} 0 & \text{if } SF < 0 \\ T_{\max} & \text{if } SF > 0 \end{cases} \tag{3.42}$$

The thrust vector $\vec{T}$ is defined through the thrust elevation angle α_T and heading angle β_T, which respectively control the in-plane and out-of-plane components:

$$\vec{T} = \begin{bmatrix} T_u \\ T_v \\ T_w \end{bmatrix} = T \begin{bmatrix} \sin \alpha_T \\ \cos \alpha_T \cos \beta_T \\ \cos \alpha_T \sin \beta_T \end{bmatrix} \tag{3.43}$$

To determine the optimal direction of the thrust vector, the Hamiltonian (3.40) is differentiated with respect to the thrust angles:

$$\frac{\partial H}{\partial \alpha_T} = 0 = \lambda_v \cos \alpha_T - (\lambda_u \cos \beta_T + \lambda_w \sin \beta_T) \sin \alpha_T \tag{3.44a}$$

$$\frac{\partial H}{\partial \beta_T} = 0 = -\lambda_u \sin \beta_T + \lambda_w \cos \beta_T \tag{3.44b}$$

Solving the above system yields the following relations:

$$\sin \alpha_T = \frac{\lambda_u}{\lambda_v} \tag{3.45a}$$

$$\cos \alpha_T \cos \beta_T = \frac{\lambda_v}{\lambda_V} \tag{3.45b}$$

$$\cos \alpha_T \sin \beta_T = \frac{\lambda_w}{\lambda_V} \tag{3.45c}$$

These quantities correspond to the direction cosines of the primer vector and are therefore consistent with the thrust components already defined in equation (3.43).

Chapter 4

Results of the orbit lowering optimization

4.1 Mission configuration and numerical framework

In this chapter, the configuration adopted for the mission scenario under investigation is presented, with particular attention to the characteristics of the satellite and the electric propulsion system. The results of the numerical simulations, performed in a Python environment, are also discussed. The objective is to achieve an orbital lowering of 10 km starting from the nominal deployment altitude of 500 km.

Two case studies are considered:

- **Ideal scenario:** the satellite dynamics are propagated under the sole effect of the central gravitational field, neglecting all orbital perturbations.
- **Perturbed scenario:** atmospheric drag is included, modelled through the interpolation of a previously collected dataset.

The first simulation step consists of a 300 m altitude reduction starting from 500 km. Once the initial conditions yielding a convergent solution are obtained, the trajectory is propagated until the target orbital altitude is reached.

The main parameters of the satellite and the electric propulsion system adopted in this study are reported in Table 4.1.

The initial scenario considers the satellite deployed at an altitude of 500 km on a circular and equatorial orbit. The orbital lowering manoeuvre is performed without altering the orbital plane inclination and follows a two-arc strategy. In the first arc, the engine ignition generates a radial velocity component that drives

Table 4.1: Main parameters of the satellite and electric propulsion system.

Vehicle	
Mass M	500 kg
Drag coefficient C_d	2.2
Cross-sectional area A	1 m^2
Ion Thruster	
Thrust T	0.025 N
Specific impulse I_{sp}	2000 s

the spacecraft towards lower altitudes. During the subsequent coasting arc, the tangential velocity increases while the radial velocity approaches zero.

The engine ignition and shutdown are governed by the Switching Function (SF): when the function is positive, the thrust is set to its maximum value, whereas for negative values the thrust is set to zero, as no thrust modulation is considered in this study.

A second strategy based on a three-arc profile is also analysed. In this case, a final thrusting phase is employed after the lowering manoeuvre to circularise the arrival orbit. At the end of the first manoeuvre, the final state of the spacecraft is stored and used as the initial condition for the subsequent propagation. In this phase, the engine remains switched off, and the same numerical integrator and atmospheric drag model employed during the manoeuvre are used.

To simplify the numerical analysis and avoid handling very large quantities, a dimensionless formulation was adopted. The orbital radius was normalised using the Earth's mean radius $R_\oplus = 6371$ km, while the velocity components u, v, and w, as well as the effective exhaust velocity, were scaled by the orbital velocity at the Earth's surface, defined as

$$v_\oplus = \sqrt{\frac{\mu_\oplus}{R_\oplus}} = 7.909 \text{ km/s}.$$

Time was non-dimensionalised using the characteristic parameter

$$T = \frac{R_\oplus}{v_\oplus},$$

and the satellite mass was selected as the reference mass unit.

A characteristic acceleration,

$$a = \frac{v_\oplus^2}{R_\oplus},$$

was introduced to render derived quantities dimensionless, such as the thrust, which was expressed relative to the product between the satellite mass and the characteristic acceleration. All other physical quantities were made dimensionless through suitable combinations of the fundamental scaling parameters defined above, ensuring consistency and simplifying the interpretation of the results.

4.1.1 The OCULUS interface

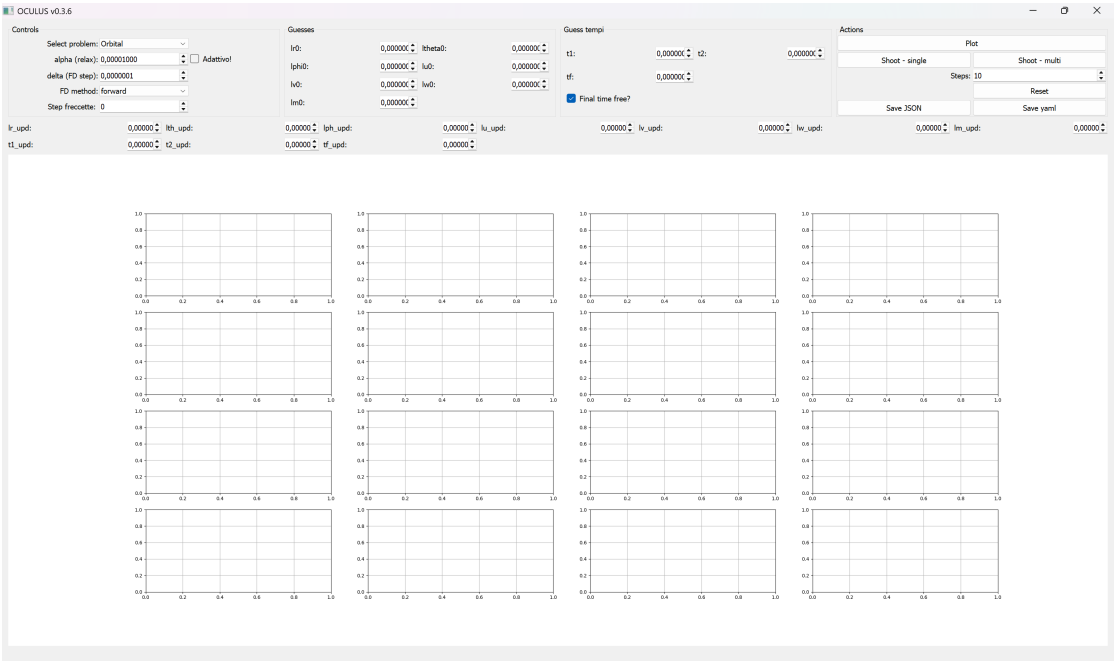

Figure 4.1: Graphical user interface

The algorithms developed in the Python environment were accessed through a graphical user interface (GUI). The availability of such a tool is fundamental when dealing with indirect methods for solving optimal-control problems: the simulation process requires the selection of numerical values for a set of initial parameters, namely the adjoint variables or costates, which are uniquely associated with the parameters comprising the satellite state. The appropriateness of the selected costate values determines the success of the simulation and the attainment of a valid solution. Having a GUI that allows convenient real-time visualisation of the evolution of states and costates with respect to the choice of initial guesses significantly optimises and accelerates the process, thereby enabling efficient investigation of multiple operational scenarios.

In addition to the initial parameters mentioned above, it is necessary to set the switching times between arcs and the overall mission duration. Among the functionalities provided by the GUI is the option to choose between a fixed-time simulation, where the mission duration is prescribed a priori, and a variable-time simulation, in which the duration is optimised within the simulation process. When selecting the latter, the Hamiltonian H emerges as the costate associated with time, and the optimisation process also includes this variable in order to maximise the performance index, ultimately yielding minimum propellant consumption.

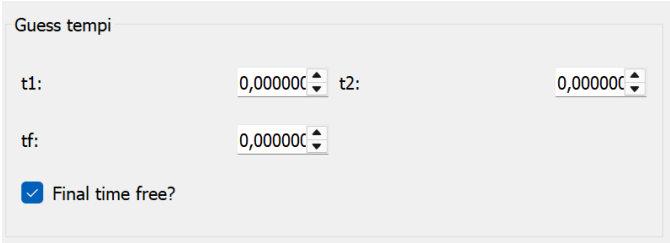

Figure 4.2: Choice between fixed-time and free-final-time simulation

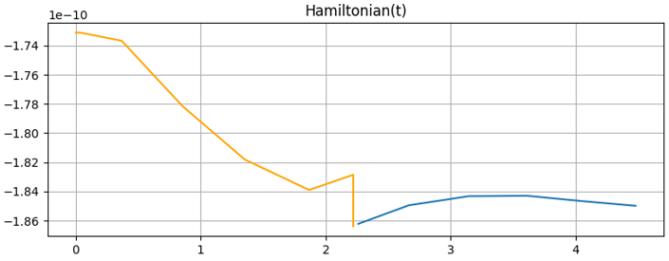

Figure 4.3: Hamiltonian evolution along the trajectory

Through the interface, several parameters regulating the differential-correction process can also be configured. By selecting higher or lower values of the relaxation parameter α, the magnitude of the correction applied at each simulation step may be adjusted. Higher values of α may lead to faster convergence when the initial costate guess is near the optimum; however, they also increase the risk that the simulation undertakes incorrect correction strategies, causing errors to diverge. One of the functions implemented in the GUI enables adaptive control of the correction process, removing this risk by adjusting the value of α based on the error history of previous steps.

This tool evolved continuously throughout the thesis work, adapting to the challenges and requirements encountered during the various simulation phases, eventually leading to the final version named *OCULUS*, [19]. Developed and presented by supervisor Luigi Mascolo at the 76th International Astronautical Congress (IAC)

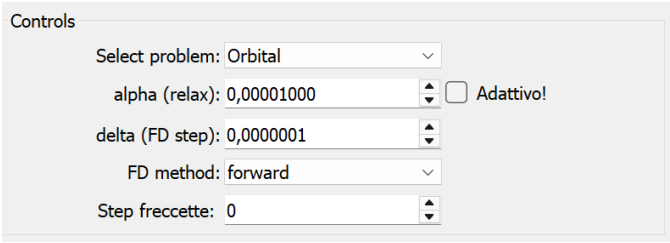

Figure 4.4: Selection of the differential-correction relaxation parameter

in Sydney, Australia, in October 2025 , this latest release significantly improved the robustness of the differential-correction process, enabling smoother convergence and reducing the likelihood of error divergence. As a result, larger relaxation parameters could be employed to reach the solution in fewer simulation steps. The most recent version also introduced the capability to individually override costates between successive steps, allowing selective intervention on specific mission components. Although the user's ability to identify appropriate initial guesses for the adjoint variables remains essential, the improvements implemented in this latest GUI version have substantially enhanced its usability.

4.2 Ideal dynamics: gravity-only scenario

As a reference scenario, the optimal control problem was initially solved in an ideal two-body environment, neglecting atmospheric drag. Under these assumptions, the spacecraft dynamics are governed solely by Earth's central gravitational field and a continuous low-thrust acceleration of constant magnitude $T_{\max}$. The thrust direction is determined according to the Pontryagin Minimum Principle, introduced in Section 3.2.2 and applied to the thrust direction formulation in Section 3.5.

Table 4.2: Initial state of the spacecraft expressed in dimensionless form.

Variable	Value
r	1.0784806152880237
θ	0.0
ϕ	0.0
u	0.0
v	0.9629280287694013
w	0.0
m	1.0

Table 4.2 reports the dimensionless initial conditions of the state variables, while Table 4.3 lists the initial values of the costates together with the switching times and the final time required to ensure convergence of the solution.

Table 4.3: Initial values of costates and switching times.

Variable	Value
$\boldsymbol{\lambda}_r$	-0.321760
$\boldsymbol{\lambda}_\theta$	0.149470
$\boldsymbol{\lambda}_\phi$	0.0
$\boldsymbol{\lambda}_u$	-0.032028
$\boldsymbol{\lambda}_v$	-0.396070
$\boldsymbol{\lambda}_w$	0.0
$\boldsymbol{\lambda}_m$	0.999540
$\boldsymbol{t}_1$	1.97
$\boldsymbol{t}_2$	3.37
$\boldsymbol{t}_f$	5.40

Figure 4.5 illustrates the behaviour of the state variables and their corresponding costates during the manoeuvre. The plots distinguish the thrust phase from the coasting phase: the orange segments indicate intervals in which the electric thruster is active, whereas the blue segments represent periods of unforced motion with zero thrust. Each manoeuvre performed using the electric propulsion system follows this recurring structure, characterised by alternating thrust-on and thrust-off arcs.

The manoeuvre is performed using a three-arc strategy of the form [1, 0, 1], where 1 denotes an active thrust phase and 0 indicates a coasting phase. Dividing the manoeuvre into thrusting and coasting arcs allows propellant savings in portions of the trajectory where thrust is not required; additionally, this strategy provides thermal benefits, as the interruption of thrusting between successive ignition phases allows the propulsion system to cool down, preventing overheating due to prolonged continuous operation.

The inverted bell-shaped profile of the switching function observed in the Figure 4.6 results from a tailored selection of the initial costate values, and is consistent with the adopted control strategy.

The values of the initial costates also provide additional insight into the mission. The costates associated with the radial position, λ_r, and with the tangential velocity, λ_v, exhibit larger magnitudes compared to the other components. This behaviour reflects the nature of the manoeuvre, in which the orbital lowering and subsequent circularisation are primarily achieved through significant variations in r and v. By

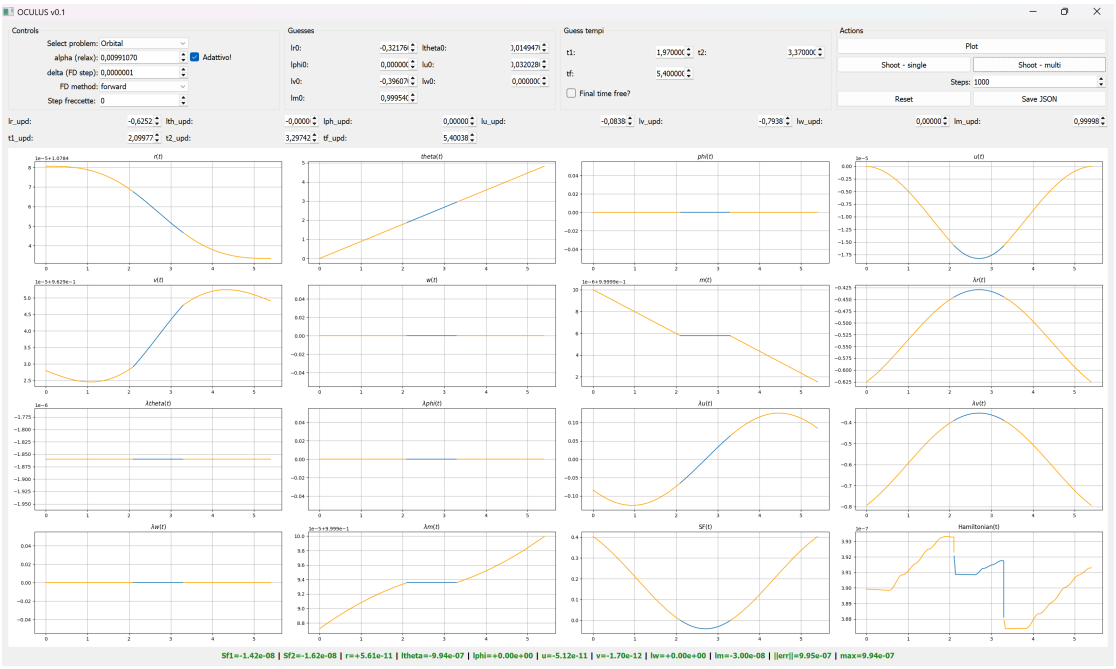

Figure 4.5: Evolution of states and costates in an ideal two-body environment

setting λ_ϕ and λ_w equal to zero, the manoeuvre is confined to the initial orbital plane, as confirmed by the behaviour of ϕ and w shown in the Figure 4.7.

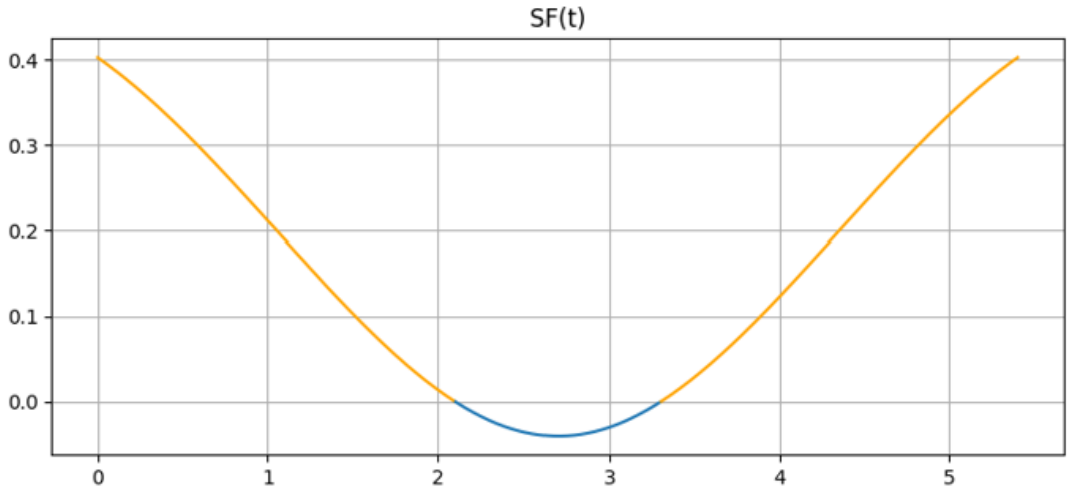

Figure 4.6: Evolution of the switching function along the trajectory

The type of manoeuvre to be performed is defined through the choice of the

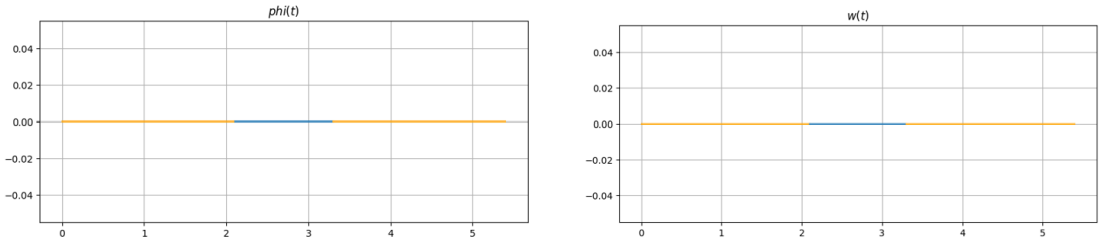

(a) ϕ **(b)** w

Figure 4.7: Out-of-plane components ϕ and w remain zero throughout the manoeuvre, confirming coplanarity.

boundary conditions, shown in the Table 4.4. The prescribed value of the orbital radius enables a 300 m altitude reduction, whereas the boundary conditions imposed on the radial and tangential velocities ensure the circularisation of the orbit at the desired altitude. Setting the costate values in the boundary conditions to zero leaves the optimisation process free to determine the corresponding variables, subject solely to the objective of maximising the performance index. Conversely, assigning a value of one to a costate in the boundary conditions indicates that the associated variable is to be maximised.

Table 4.4: Boundary conditions of the spacecraft (dimensionless).

Variable	Value
r	1.078433526918851
λ_θ	0.0
λ_ϕ	0.0
u	0.0
v	0.9629490510273464
λ_w	0.0
λ_m	1.0

The boundary condition (BC) residuals are reported in Table 4.5. All components exhibit magnitudes on the order of 10^{-7}–10^{-8}, which are well within the adopted numerical tolerance. In particular, the residuals associated with λ_ϕ and λ_w vanish identically, while those of the remaining variables remain negligible. The computed error norm is 2.74×10^{-7}, below the convergence threshold of 10^{-6}, thus satisfying the required criterion. These results confirm that the boundary conditions are met with high accuracy and that the resulting numerical solution is consistent.

Finally, the Table 4.6 presents the final state reached by the spacecraft at

Table 4.5: Residual boundary condition errors at convergence.

Variable	Value
$\Delta \mathrm{SF}_1$	$1.22416332 \times 10^{-7}$
$\Delta \mathrm{SF}_2$	$2.17321542 \times 10^{-7}$
Δr	$1.66890695 \times 10^{-8}$
$\Delta \lambda_\theta$	$-2.73698367 \times 10^{-7}$
$\Delta \lambda_\phi$	$6.04199748 \times 10^{-17}$
Δu	$-6.65842874 \times 10^{-8}$
Δv	$2.45572555 \times 10^{-8}$
$\Delta \lambda_w$	$-1.13686506 \times 10^{-16}$
$\Delta \lambda_m$	$1.80738313 \times 10^{-10}$
$\|\mathrm{err}\|$	$2.72944209 \times 10^{-7}$
max_err	$2.73698367 \times 10^{-7}$

the end of the manoeuvre, summarising the resulting orbital configuration. This representation is useful to assess the effectiveness of the manoeuvre and to quantify the variations induced with respect to the initial conditions.

Table 4.6: Final state of the spacecraft at the end of the manoeuvre (dimensionless).

Variable	Value
r	1.0784335436079162
θ	4.797825739006499
ϕ	0.0
u	$-6.658428837814118 \times 10^{-8}$
v	0.9629490755846027
w	0.0
m	0.9999915074055511

4.3 Perturbed dynamics: atmospheric drag scenario

In this section, the orbit-lowering manoeuvre is analysed in a perturbed environment where the effects of atmospheric drag are taken into account. Unlike the gravity-only scenario discussed in the previous section, the spacecraft is now subject to

a dissipative force that continuously reduces its orbital energy, resulting in a gradual decay of the orbital radius. The atmospheric density is obtained through interpolation from a precomputed dataset, and the drag acceleration is evaluated using the aerodynamic model described in Section 2.4.1.

The presence of atmospheric drag significantly alters the structure of the optimal trajectory: in addition to the control-driven decrease in altitude, a portion of the orbital decay is achieved passively through dissipative effects, reducing the required propellant consumption. The following analysis highlights these differences and quantifies the contribution of drag to the overall manoeuvre performance.

To characterise the effects of drag on the orbital decay, the following subsection presents the resulting trajectory and compares it with the ideal scenario.

Two different cases are analysed. In the first part, a comparison is carried out for a 300 m orbit-lowering manoeuvre using the three-arc strategy, highlighting the lower propellant consumption observed in the perturbed case, where atmospheric drag contributes passively to the reduction of orbital energy.

In the second part, a different manoeuvre strategy is considered. A two-arc profile of the type [1,0] is adopted: the spacecraft is first lowered to an altitude of 499.7 km, after which the resulting state is propagated until the orbital radius reaches the target altitude of 490 km. This analysis highlights how modifying the optimal strategy affects propellant consumption.

4.3.1 Three-arc strategy and comparison with ideal case

This section reports the simulation results for the perturbed environment. The adopted manoeuvre retains the three-arc structure used in the ideal case, but the spacecraft dynamics have been extended to account for atmospheric drag. The initial state of the spacecraft and the boundary conditions are the same as in the ideal case and are omitted here for conciseness. The Table 4.7 presents the initial costate values that enabled convergence, along with their corresponding values at the end of the simulation. To allow a direct comparison with the ideal scenario, the final state of the spacecraft at the end of the manoeuvre is also reported.

By comparing Table 4.6 with Table 4.8, a reduction in propellant consumption can be observed. The limited magnitude of this saving is primarily due to the relatively weak effect of atmospheric drag at the considered altitude, as well as to the short duration of the manoeuvre.

For the same reasons, the overall dynamical behaviour of the spacecraft remains largely unchanged, as can be observed in Figure 4.8. The first thrust arc is required to induce a non-zero radial velocity component, steering the spacecraft towards lower orbital radii. At the beginning of the first arc, the tangential velocity undergoes a slight decrease, followed by an increase towards the end of the burn.

Table 4.7: Initial and converged values of costates and switching times (dimensionless).

Variable	Initial guess	Updated values at convergence
$\boldsymbol{\lambda_r}$	-0.62523	-0.624869065
$\boldsymbol{\lambda_\theta}$	-9.94×10^{-7}	9.95×10^{-7}
$\boldsymbol{\lambda_\phi}$	0.0	0.0
$\boldsymbol{\lambda_u}$	-0.083881	-0.083907281
$\boldsymbol{\lambda_v}$	-0.79387	-0.79342063
$\boldsymbol{\lambda_w}$	0.0	0.0
$\boldsymbol{\lambda_m}$	0.99999	0.999987255
$\boldsymbol{t_1}$	2.09	2.099027361
$\boldsymbol{t_2}$	3.29	3.300683081
$\boldsymbol{t_f}$	5.39	5.399756464

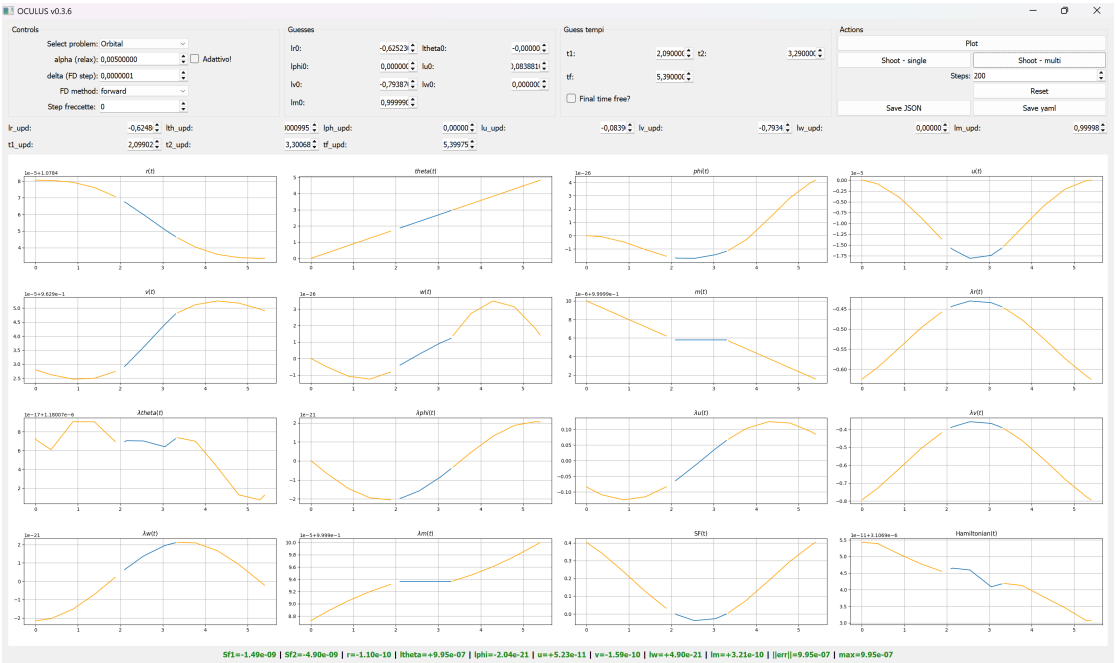

Figure 4.8: State and costate evolution during the manoeuvre

During the coast phase, v continues to increase, while the magnitude of u reverses trend and progressively decreases.

The final thrust arc performs orbit circularisation: the radial component u is driven back to zero, whereas v converges to the value associated with a circular

orbit at the final altitude. The persistence of the adopted strategy is also evident from the switching function, whose shape remains essentially unchanged.

Table 4.8: Final state of the spacecraft at the end of the manoeuvre (dimensionless).

Variable	Value
r	1.0784335268092544
θ	4.821363545812885
ϕ	0.0
u	$5.228997207043773 \times 10^{-11}$
v	0.9629490508684441
w	0.0
m	0.9999915465181319

During each burn, the spacecraft mass exhibits a linear decrease, in accordance with the mass flow rate formulation of Eq.3.38, which results from operating the thruster at constant maximum thrust. This trend can be observed in Figure 4.9.

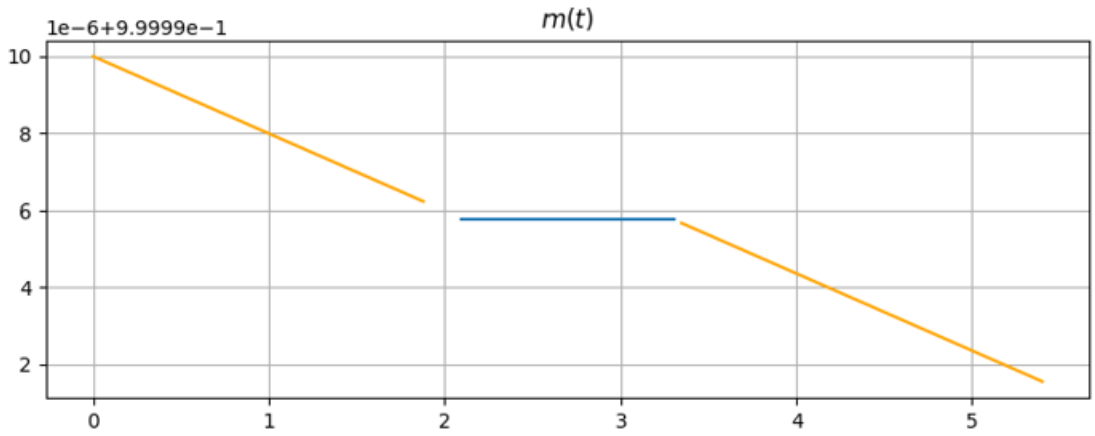

Figure 4.9: Mass depletion profile during the orbit-lowering manoeuvre.

Although atmospheric drag is typically regarded as a detrimental perturbation in orbit maintenance problems, its effect in an orbit-lowering manoeuvre is fundamentally different. In the present case, drag contributes passively to the reduction of orbital energy and therefore reduces the thrust effort required to achieve the target altitude. As a result, a slight reduction in propellant consumption is observed in the drag-perturbed scenario compared to the ideal case.

4.3.2 Orbit-lowering manoeuvre under atmospheric drag: two-arc strategy

This section presents the full orbit-lowering manoeuvre down to the target altitude of 490 km. The mission begins with a 300-meter descent manoeuvre, followed by an unforced propagation phase that brings the spacecraft to its final orbit. The first phase adopts a revised thrusting strategy, primarily aimed at further reducing propellant consumption.

In this configuration, the terminal state of the first manoeuvre serves as the initial condition for the propagation phase. Since intermediate orbit circularisation is no longer required, the second burn is omitted and a two-arc strategy [1,0] is adopted.

Table 4.9: Initial state of the spacecraft at the beginning of the manoeuvre (dimensionless).

Variable	Value
r	1.0784806152880237
θ	0.0
ϕ	0.0
u	0.0
v	0.9629280287694013
w	0.0
m	1.0

Table 4.10: Initial and converged values of costates and switching times (dimensionless).

Variable	Initial guess	Updated values at convergence
$\boldsymbol{\lambda_r}$	-0.3057	-0.312141997
$\boldsymbol{\lambda_\theta}$	0.0	-2.97×10^{-7}
$\boldsymbol{\lambda_\phi}$	0.0	0.0
$\boldsymbol{\lambda_u}$	0.1069	0.099652286
$\boldsymbol{\lambda_v}$	-0.3853	-0.435752218
$\boldsymbol{\lambda_w}$	0.0	0.0
$\boldsymbol{\lambda_m}$	0.99999	0.999994462
$\boldsymbol{t_1}$	1.5	2.220044122
$\boldsymbol{t_f}$	4.25	4.479334115

The manoeuvre starts from a circular orbit at an altitude of 500 km. The initial spacecraft state is provided in Table 4.9, whereas the set of initial costates leading to the converged solution is reported in Table 4.10. The costates λ_r and λ_v exhibit substantially higher magnitudes compared to the remaining costates, implying that the optimisation places greater emphasis on modifying the associated state variables. The table also illustrates the evolution of the costate values. As the simulation was carried out with a free final time, the mission duration was optimised together with the other parameters to maximise propellant savings. The two-arc manoeuvre has a total duration of approximately 60 minutes, making it faster than the three-arc strategy, which requires 72 minutes.

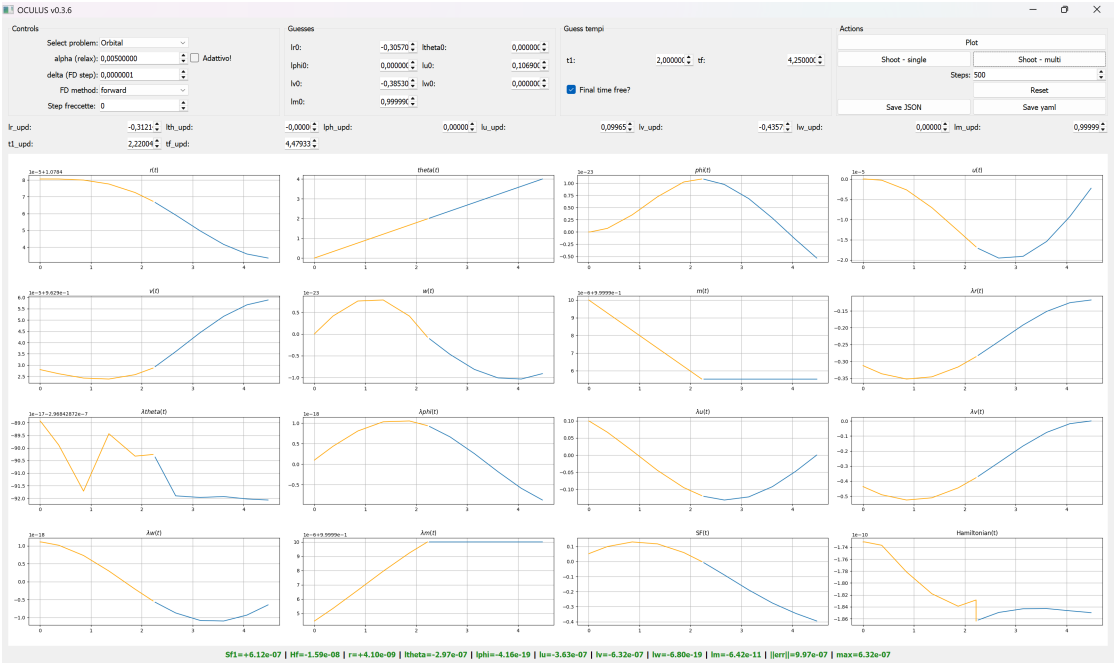

Figure 4.10: State and costate evolution during the drag-perturbed orbit-lowering manoeuvre

Figure 4.10 illustrates the final results of the simulation, whereas Table 4.11 reports the spacecraft's final state at the end of the manoeuvre.

The mass evolution associated with the two-arc strategy, shown in Figure 4.11, clearly highlights a reduction in propellant consumption compared to the three-arc manoeuvre. This improvement is significantly more pronounced than the difference observed between the ideal and drag-perturbed scenarios, as the manoeuvre duration is relatively short and the effect of atmospheric drag at the considered operative altitude remains limited. Consequently, the choice of the thrusting strategy plays a dominant role in determining the overall propellant expenditure.

Table 4.11: Final state of the spacecraft at the end of the manoeuvre (dimensionless).

Variable	Value
r	1.0784335310150008
θ	3.9995020477835443
ϕ	0.0
u	$-2.252019802390247 \times 10^{-6}$
v	0.962958871940314
w	0.0
m	0.9999955296206842

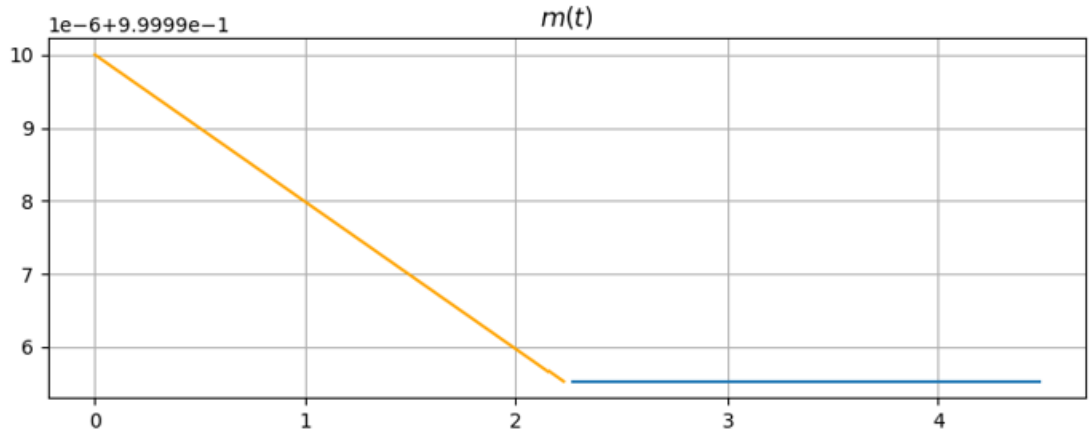

Figure 4.11: Spacecraft mass evolution during the two-arc orbit-lowering manoeuvre.

Propagation and orbital decay

At the end of the first phase, the final state is extracted and used as the initial condition for the second phase. The propagation is performed in a Python environment using a dedicated script. The same numerical integrator adopted in the first phase is employed, with the thrust set to zero throughout the propagation. The results of the propagation phase are shown in Figure 4.12, illustrating the evolution of the orbital radius down to the target altitude.

A more detailed inspection of the dimensionless radius reveals oscillations between a minimum and a maximum value, reflecting the fact that the spacecraft no longer follows a perfectly circular orbit as in the initial condition. By evaluating the radii at apogee and perigee, the orbital eccentricity can be computed, yielding

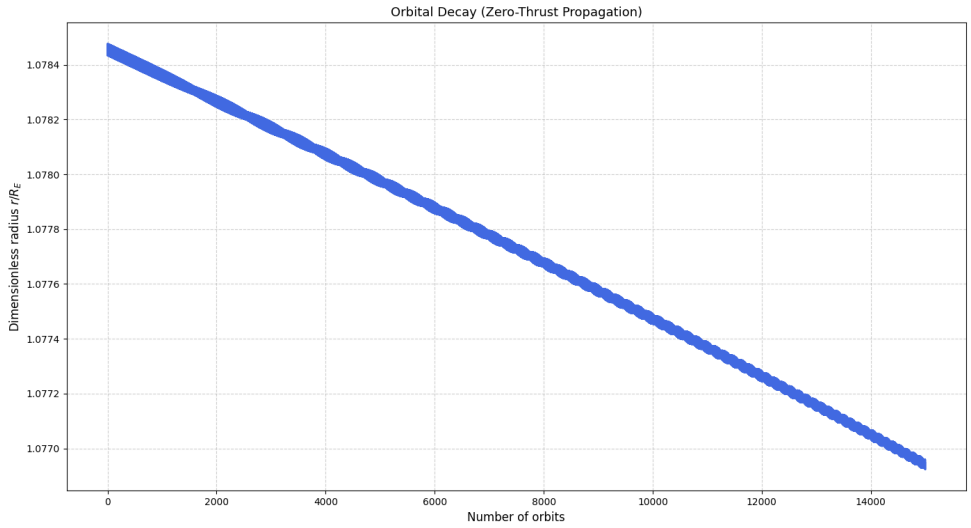

Figure 4.12: Unforced propagation phase following the initial 300 m descent, showing the gradual lowering to the target altitude of 490 km.

a value of $e = 1.5299 \times 10^{-5}$.

The results of the propagation phase are shown below in Figure 4.14, and the corresponding final state of the spacecraft is listed in Table 4.12.

Table 4.12: Final state of the spacecraft upon reaching the target altitude (dimensionless).

Variable	**Value**
r	1.0769132769103629
θ	2.0108913350598954
ϕ	0.0
u	$-1.5698854224782358 \times 10^{-5}$
v	0.9636239021884728
w	0.0
m	0.9999955296206842

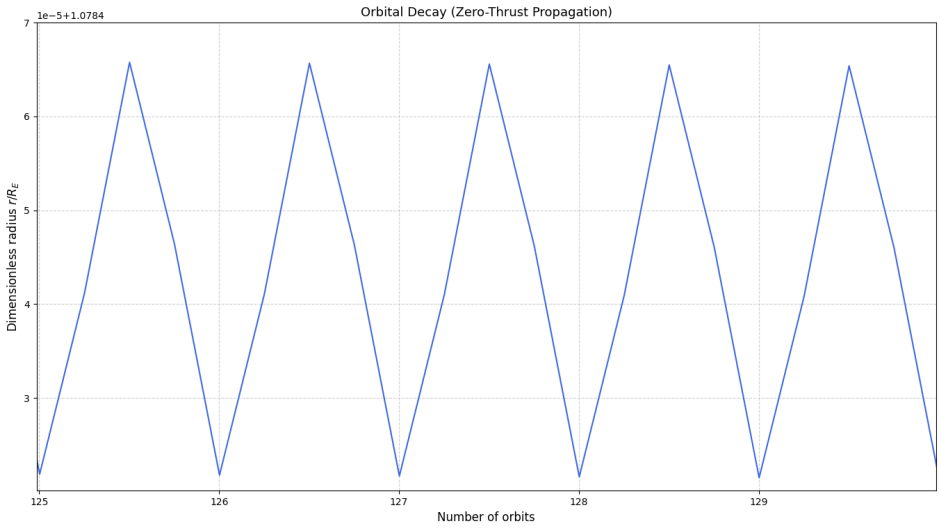

Figure 4.13: Oscillation of the orbital radius during the unforced propagation phase.

```
PS C:\Users\ACER\Desktop\Tesi\Draft_IM> C:\Users\ACER\AppData\Local\Programs\Python\Python312\python.exe c:/Users/ACER/Desktop/Tesi/Draft_IM/test
s/propagation.py
[ 1.07843353e+00  3.99950205e+00  0.00000000e+00 -2.25201980e-06
  9.62958872e-01  0.00000000e+00  9.99995530e-01  0.00000000e+00
  0.00000000e+00  0.00000000e+00  0.00000000e+00  0.00000000e+00
  0.00000000e+00  0.00000000e+00]
[108013.57043772]
La nuova quota si trova a 490.0144871959219 km
Il satellite si trova ad un angolo theta pari a 115.21558655835952°
```

Figure 4.14: Result of the propagation phase.

4.4 Overview

This section provides an overview of the main results obtained throughout the orbit-lowering analysis. The study investigated different strategies for reducing the orbital altitude of a spacecraft starting from a circular orbit at 500 km, comparing ideal and drag-perturbed scenarios as well as three-arc and two-arc thrusting profiles.

The inclusion of atmospheric drag leads to a limited but consistent reduction in propellant consumption, reflecting the relatively weak aerodynamic effects at the considered altitude and the short duration of the manoeuvres. Although the overall structure of the optimal solution remains similar to the ideal case, the presence of drag contributes passively to the orbital decay, particularly during coasting and propagation phases.

A comparison between thrusting strategies shows that reducing the number of thrust arcs can improve efficiency when orbit circularisation is not required at intermediate altitudes. In this context, the combination of an optimal control-driven descent and an unforced propagation phase proves effective in achieving the target altitude while limiting propellant usage.

Overall, the results highlight the importance of jointly considering control strategy and dynamical environment when designing orbit-lowering manoeuvres. The adopted framework demonstrates flexibility and robustness, providing a foundation for further extensions to lower altitudes, longer mission phases, and more complex dynamical models.

Chapter 5

Conclusions and future research

This thesis presented the formulation, numerical solution, and analysis of an optimal control problem for low-thrust satellite operations in Low Earth Orbit (LEO), with particular emphasis on atmosphere-induced perturbations and orbit-lowering manoeuvres. The work combines detailed dynamical modelling, indirect optimal control techniques, and a fully integrated numerical implementation developed in a Python environment and supported by a dedicated graphical user interface.

The main contributions and findings of this work can be summarised as follows:

- A comprehensive dynamical model was developed in spherical coordinates, accounting for the central gravitational attraction of the Earth and the effects of atmospheric drag. The aerodynamic perturbation was obtained through a one-dimensional interpolation of precomputed atmospheric density data, enabling an efficient yet physically consistent representation of drag effects at the considered orbital altitudes.

- The optimal control problem was formulated using Pontryagin's Minimum Principle, leading to a two-point boundary value problem. The resulting system was solved through an indirect shooting method combined with Newton iteration, providing high-accuracy solutions and valuable insight into the structure of the optimal thrusting strategy.

- A progressive set of simulations was carried out, starting from an ideal two-body scenario and extending to a drag-perturbed environment. This approach allowed a clear assessment of the role of atmospheric drag on the optimal solution, highlighting its influence on propellant consumption, mission duration, and orbital evolution.

- Different thrusting strategies were analysed and compared, including three-arc and two-arc profiles combined with unforced propagation phases. The results demonstrated that an appropriate combination of optimal control and passive orbital decay can lead to improved propellant efficiency, particularly when intermediate orbit circularisation is not required.

- A modular and extensible software framework was developed to support the modelling and optimisation process. The inclusion of a graphical user interface enhances usability, facilitates the tuning of initial guesses for the indirect method, and supports efficient visualisation and analysis of simulation results.

Overall, the results show that atmospheric drag plays a non-negligible role in low-thrust orbit-lowering manoeuvres in LEO and must be properly accounted for to obtain realistic performance estimates. Even at relatively high altitudes, drag contributes to orbital decay and affects the optimal control structure, propellant budget, and achievable mission timelines.

The methodology developed in this thesis provides a rigorous and flexible framework for preliminary mission analysis and optimisation. It constitutes a solid foundation for further extensions, including longer mission durations, lower operational altitudes, and the inclusion of additional perturbative effects relevant to realistic spacecraft operations.

5.1 Limitations and future developments

Despite the encouraging results obtained, the analysis presented in this thesis is subject to a number of modelling and methodological limitations that define possible directions for future improvements.

From a dynamical standpoint, the current formulation accounts only for the central gravitational attraction of the Earth and aerodynamic drag. Higher-order gravitational perturbations, such as the oblateness effect represented by the J_2 harmonic, are neglected. While this assumption is acceptable for short-duration manoeuvres and preliminary analyses, the inclusion of J_2 would improve the accuracy of the orbital evolution, particularly for longer simulations and lower orbital altitudes, where secular effects on the orbital elements become increasingly relevant. Similarly, the adoption of a more complex gravitational model, such as a three-body formulation including third-body perturbations, could further enhance the fidelity of the simulations and provide a more realistic representation of the operational environment.

With regard to atmospheric drag modelling, the current approach relies on a one-dimensional interpolation of precomputed atmospheric density data. Although this choice represents a reasonable compromise between accuracy and computational

efficiency, it neglects the explicit dependence of atmospheric density on epoch, solar activity, and geomagnetic conditions. The integration of a time-dependent drag model that accounts for solar flux variations, such as the NRLMSISE-00 model [17], would allow the investigation of seasonal and short-term variability in aerodynamic perturbations, leading to more robust and realistic mission analyses.

From a methodological perspective, the optimisation framework developed in this thesis focuses on single manoeuvre segments, in which a propulsive orbit-lowering phase is followed by either orbit circularisation or unforced propagation. A significant improvement would consist in the development of an automated multi-phase tool capable of alternately managing active thrusting phases (with non-zero thrust) and passive propagation phases. By iteratively repeating this sequence, it would be possible to progressively reach the target altitude with improved efficiency and reduced overall mission duration.

The key idea behind this approach is to exploit the continuity of the optimal solution: after obtaining convergence for an initial lowering manoeuvre of limited magnitude (e.g. a 300 m altitude reduction), the final state of the spacecraft would be used as the initial condition for a short unforced propagation, typically lasting a few orbital periods. At the end of the propagation, a new propulsive lowering phase would be initiated, using as initial guesses for the costates the updated values obtained at the end of the previous phase. In this way, the costates would evolve gradually through a sequence of small corrections, ensuring numerical convergence as long as the differences between consecutive phases remain sufficiently small.

Such an automated framework would effectively transform a complex long-duration orbit-lowering problem into a sequence of simpler, locally convergent subproblems. This strategy would significantly enhance the robustness of the indirect method, reduce the sensitivity to initial guesses, and enable the efficient simulation of long-term orbit decay scenarios. Ultimately, this extension would provide a powerful tool for the optimal planning of low-thrust orbit-lowering missions in realistic operational conditions.

Appendix A

Euler–Lagrange equations for the adjoint variables

In this appendix, the Euler–Lagrange equations governing the evolution of the adjoint variables are reported in both compact and component-wise form. These relations are derived from the optimal control formulation presented in Chapter 3 and follow directly from the Pontryagin Maximum Principle.

A.1 Compact form

The adjoint dynamics can be written in compact form as:

$$\dot{\boldsymbol{\lambda}} = -\frac{\partial H}{\partial \boldsymbol{x}} \tag{A.1}$$

A.2 Component-wise equations

$$\begin{aligned}\dot{\lambda}_r = {} & \frac{1}{r^2}\left[\lambda_\theta v\cos\phi + \lambda_\phi w + \lambda_u\left(-\frac{2u}{r} + v^2 + w^2\right)\right] \\ & + \frac{1}{r^2}\left[\lambda_v(-uv + vw\tan\phi) + \lambda_w(-uv - v^2\tan\phi)\right] \\ & - \lambda_u\frac{\partial(a_p)_u}{\partial r} - \lambda_v\frac{\partial(a_p)_v}{\partial r} - \lambda_w\frac{\partial(a_p)_w}{\partial r} - \mathrm{SF}\frac{\partial T}{\partial r}\end{aligned} \tag{A.2}$$

$$\dot{\lambda}_\theta = -\lambda_u\frac{\partial(a_p)_u}{\partial \theta} - \lambda_v\frac{\partial(a_p)_v}{\partial \theta} - \lambda_w\frac{\partial(a_p)_w}{\partial \theta} + \mathrm{SF}\frac{\partial T}{\partial \theta} \tag{A.3}$$

$$\dot{\lambda}_\phi = \frac{1}{r\cos^2\phi}\Big(- \lambda_\theta v\sin\phi - \lambda_u vw + \lambda_v w + \lambda_w v^2\Big) - \lambda_u\frac{\partial(a_p)_u}{\partial\phi} - \lambda_v\frac{\partial(a_p)_v}{\partial\phi} - \lambda_w\frac{\partial(a_p)_w}{\partial\phi} + \mathrm{SF}\frac{\partial T}{\partial\phi} \tag{A.4}$$

$$\dot{\lambda}_u = \frac{1}{r}\Big(- \lambda_r r + \lambda_u v + \lambda_w w\Big) \tag{A.5}$$

$$\dot{\lambda}_v = \frac{1}{r}\Big(- \frac{\lambda_\theta}{\cos\phi} - 2\lambda_u v + \lambda_u(u - w\tan\phi) + 2\lambda_w v\tan\phi\Big) \tag{A.6}$$

$$\dot{\lambda}_w = \frac{1}{r}\Big(- \lambda_\phi - 2\lambda_u w - \lambda_v v\tan\phi + \lambda_w u\Big) \tag{A.7}$$

$$\dot{\lambda}_m = \frac{T}{m^2}\lambda_v - \lambda_u\frac{\partial(a_p)_u}{\partial m} - \lambda_v\frac{\partial(a_p)_v}{\partial m} - \lambda_w\frac{\partial(a_p)_w}{\partial m} \tag{A.8}$$

Bibliography

[1] Luigi Mascolo. «Low-Thrust Optimal Escape Trajectories from Lagrangian Points and Quasi-Periodic Orbits in a High-Fidelity Model». Tesi di dottorato, archivio IRIS, accesso aperto: https://hdl.handle.net/11583/2976595. PhD thesis. Politecnico di Torino, Feb. 2023 (cit. on pp. viii, 8, 18, 24, 27).

[2] G. March, E. Doornbos, P. N. A. M. Visser, and J. A. Encarnacao. «High-fidelity geometry models for improving the consistency of CHAMP, GRACE, GOCE and Swarm thermospheric density data sets». In: *Advances in Space Research* 62.1 (2018), pp. 296–314. DOI: 10.1016/j.asr.2018.04.017 (cit. on pp. 3, 4).

[3] European Space Agency. *Improved resolution for SkySat data via orbit lowering from 500 km to 450 km*. Accessed: 2025-08-26. 2020. URL: https://earth.esa.int/eogateway/news/improved-resolution-for-skysat-data-and-extension-of-planet-data-availability (cit. on p. 3).

[4] Planet Labs. *SkySat 50 cm FAQ: lowering of SkySat orbit to 450 km in early 2020*. Accessed: 2025-08-26. 2020. URL: https://support.planet.com/hc/en-us/articles/360010635857-SkySat-50cm-FAQ (cit. on p. 3).

[5] European Space Agency. *GOCE mission operations overview*. Accessed: 2025-08-26. 2013. URL: https://www.esa.int/Enabling_Support/Operations/GOCE (cit. on pp. 3, 5).

[6] N. H. Crisp, P. C. E. Roberts, S. Livadiotti, et al. «The Benefits of Very Low Earth Orbit for Earth Observation Missions». In: *arXiv preprint arXiv:2007.07699* (2020). Accessed: 2025-08-26. URL: https://arxiv.org/abs/2007.07699 (cit. on pp. 4, 5).

[7] X. Chi, Y. Huang, B. Hu, Y. Li, and Y. Zhang. «Advocating Very Low Earth Orbit as the Next Frontier for Satellite Operations». In: *Space Digitalization Conference (SDC) 2021*. Accessed: 2025-08-26. 2021. URL: https://conference.sdo.esoc.esa.int/proceedings/sdc8/paper/109/SDC8-paper109.pdf (cit. on p. 4).

[8] European Defence Agency. *LEO2VLEO initiative: manoeuvring satellite constellation from LEO into VLEO*. Accessed: 2025-08-26. 2022. URL: https://www.eda.europa.eu/projects-and-operations/project.html?node_number=613 (cit. on pp. 4, 6).

[9] Y. Jiang, X. Liu, Z. Wang, and Y. Chen. «Aerodynamic drag analysis and reduction strategy for VLEO satellites». In: *Acta Astronautica* (2023). DOI: 10.1016/j.actaastro.2022.09.051. URL: https://www.sciencedirect.com/science/article/abs/pii/S0094576522007519 (cit. on p. 4).

[10] S. T. King and M. L. R. Walker. «Small Satellite LEO Maneuvers with Low-Power Electric Propulsion». In: *AIAA/USU Conference on Small Satellites*. Accessed: 2025-08-26. 2008. URL: https://hpepl.ae.gatech.edu/papers/AIAA-2008-4516.pdf (cit. on p. 5).

[11] I. Levchenko, S. Xu, G. Teel, D. Mariotti, M. L. R. Walker, and M. Keidar. «Recent progress and perspectives of space electric propulsion systems based on smart nanomaterials». In: *Nature Communications* 9.1 (2018), p. 879. DOI: 10.1038/s41467-017-02269-7. URL: https://doi.org/10.1038/s41467-017-02269-7 (cit. on p. 5).

[12] Inter-Agency Space Debris Coordination Committee. *IADC Space Debris Mitigation Guidelines*. Tech. rep. Accessed: 2025-08-26. IADC, 2007. URL: https://www.unoosa.org/pdf/publications/st_space_49E.pdf (cit. on p. 5).

[13] European Space Agency. *GOCE End-of-Mission Operations Report*. Tech. rep. Accessed: 2025-10-23. European Space Agency (ESA), 2014. URL: https://earth.esa.int/eogateway/documents/20142/0/GOCE-End-of-Mission-Operations-Report.pdf (cit. on p. 6).

[14] European Space Agency. *Swarm satellites' orbit configuration and mission operations*. Accessed: 2025-08-26. 2013. URL: https://www.esa.int/Enabling_Support/Operations/Swarm_operations (cit. on p. 6).

[15] Roger R. Bate, Donald D. Mueller, and Jerry E. White. *Fundamentals of Astrodynamics*. Dover Publications, 1971. ISBN: 978-0486600611 (cit. on p. 9).

[16] Karel F. Wakker. *Fundamentals of Astrodynamics*. Institutional Repository Library, Delft University of Technology, Delft, The Netherlands, 2015. ISBN: 978-94-6186-419-2 (cit. on pp. 13, 14).

[17] J. M. Picone, A. E. Hedin, D. P. Drob, and A. C. Aikin. «NRLMSISE-00 empirical model of the atmosphere: Statistical comparisons and scientific issues». In: *Journal of Geophysical Research: Space Physics* 107.A12 (2002), p. 1468. DOI: 10.1029/2002JA009430 (cit. on p. 52).

[18] Alessandro Zavoli. «Indirect Optimization of Bang-Bang Control Problems and Applications to Formation Flying Missions». PhD thesis. Sapienza, Università di Roma, May 2013. URL: https://iris.uniroma1.it/retrieve/e3835315-d387-15e8-e053-a505fe0a3de9/Alessandro%20Zavoli%20-%20PhD%20thesis%20-%20Ciclo%20XXV%20-%20padis.pdf (cit. on p. 18).

[19] Luigi Mascolo. «OCULUS – A unified visual solver for Optimal Control Problems via indirect methods». In: *Proceedings of the 76th International Astronautical Congress (IAC)*. Accessed online. Sydney, Australia: International Astronautical Federation, 2025. URL: https://www.researchgate.net/publication/396514981_OCULUS_-A_unified_visual_solver_for_Optimal_Control_Problems_via_indirect_methods (cit. on p. 35).